

1 **Nanobodies combined with DNA-PAINT super-resolution reveal a staggered titin nano-**
2 **architecture in flight muscles**

3

4 Florian Schueder^{1,2*}, Pierre Mangeol^{3*}, Eunice HoYee Chan³, Renate Rees⁴, Jürgen
5 Schünemann⁴, Ralf Jungmann^{1,2}, Dirk Görlich⁴, Frank Schnorrer³

6

7

8 ¹ Faculty of Physics and Center for Nanoscience, Ludwig Maximilian University, 80539
9 Munich, Germany

10 ² Max Planck Institute of Biochemistry, 82152 Martinsried, Germany

11 ³ Aix Marseille University, CNRS, IBDM, Turing Centre for Living Systems, 13288
12 Marseille, France

13 ⁴ Max Planck Institute for Multidisciplinary Sciences, Göttingen, Germany

14

15 * Equal contribution

16

17 Correspondence:

18 goerlich@mpinat.mpg.de

19 jungmann@biochem.mpg.de

20 frank.schnorrer@univ-amu.fr

21

22 keywords: muscle; sarcomere; myofibril; *Drosophila*; titin; mechanics; DNA-PAINT;
23 nanobodies; super-resolution;

24

25

26 **Abstract**

27 **Sarcomeres are the force producing units of all striated muscles. Their**
28 **nanoarchitecture critically depends on the large titin protein, which in vertebrates**
29 **spans from the sarcomeric Z-disc to the M-band and hence links actin and myosin**
30 **filaments stably together. This ensures sarcomeric integrity and determines the length**
31 **of vertebrate sarcomeres. However, the instructive role of titins for sarcomeric**
32 **architecture outside of vertebrates is not as well understood. Here, we used a series of**
33 **nanobodies, the *Drosophila* titin nanobody toolbox, recognising specific domains of the**
34 **two *Drosophila* titin homologs Sallimus and Projectin to determine their precise**
35 **location in intact flight muscles. By combining nanobodies with DNA-PAINT super-**
36 **resolution microscopy, we found that, similar to vertebrate titin, Sallimus bridges**
37 **across the flight muscle I-band, whereas Projectin is located at the beginning of the A-**
38 **band. Interestingly, the ends of both proteins overlap at the I-band/A-band border,**
39 **revealing a staggered organisation of the two *Drosophila* titin homologs. This**
40 **architecture may help to stably anchor Sallimus at the myosin filament and hence**
41 **ensure efficient force transduction during flight.**

42

43 **Introduction**

44 Skeletal and heart muscles produce forces that power body movements and fluid flow in
45 animals. These forces are produced by conserved macromolecular machines called
46 sarcomeres. Sarcomeres are organised into long periodic chains called myofibrils that
47 mechanically span the entire muscle fiber length and thus sarcomere contraction results in
48 muscle contraction (Gautel, 2011; Huxley, 1969; Lemke and Schnorrer, 2017).

49 The sarcomeric architecture is conserved in striated muscles across animals.
50 Sarcomeres are bordered by two Z-discs, which anchor the plus ends of parallel actin
51 filaments. These extend towards the centrally located bipolar myosin filaments that are cross-
52 linked at the M-band of the sarcomere. In vertebrate sarcomeres, actin and myosin filaments
53 are mechanically linked by the connecting filament built by the gigantic titin protein, whose
54 N-terminus is anchored to alpha-actinin at the Z-disc while its C-terminus is embedded within
55 the sarcomeric M-band. Thus, titin spans as linear protein across half a sarcomere in
56 vertebrate muscle (Gautel and Djinić-Carugo, 2016; Lange et al., 2006; Linke, 2018; Squire
57 et al., 2005). This stereotypic sarcomere architecture results in a defined sarcomere length
58 (distance between two neighbouring Z-discs), which is about 3 μm in relaxed human skeletal
59 muscle (Ehler and Gautel, 2008; Llewellyn et al., 2008; Regev et al., 2011), and is responsible
60 for the typical striated appearance of skeletal muscles.

61 The defined sarcomeric architecture sparked the ‘titin ruler hypothesis’, proposing that
62 the long titin protein rules sarcomere length in vertebrate muscles (Tskhovrebova and Trinick,
63 2012; 2017). Recently, this hypothesis has been strongly supported by *in vivo* genetic
64 evidence. Deletion of parts of titin’s flexible I-band or its stiff A-band regions in mouse
65 skeletal muscle resulted in a shortening of the sarcomeric I-band or A-band, respectively
66 (Brynnel et al., 2018; Tonino et al., 2017). Furthermore, recent evidence substantiated that
67 titin is the main sarcomeric component responsible for the passive tension of the muscle,
68 suggesting that mechanical tension present in relaxed muscle is stretching titin into its

69 extended conformation (Li et al., 2020; Linke, 2018; Rivas-Pardo et al., 2020; Swist et al.,
70 2020). Thus, titin mechanically links actin and myosin filaments together and is responsible
71 for establishing and maintaining sarcomeric architecture in vertebrate striated muscle.

72 Striated muscle architecture is not restricted to vertebrates but conserved in insects and
73 worms. However, in contrast to vertebrates, titin's role in *Drosophila* and *C. elegans* appears
74 to be split into two proteins, one containing the flexible I-band features and the other the stiff
75 A-band features of titin (Loreau et al., 2022; Tskhovrebova and Trinick, 2003). Surprisingly,
76 the sarcomere length in flies and worms is still stereotypic for the respective muscle fiber type.
77 In *Drosophila* the sarcomere length is about 3.5 μm for indirect flight muscles and about 8
78 μm for larval body wall muscles. To date, it is unclear how sarcomere length in these muscles
79 is determined. Furthermore, it is unknown how the titin homologs are precisely organised
80 within the sarcomere and if they contribute to sarcomere length regulation in insect muscle.

81 We aim to address the questions how invertebrate titin homologs instruct sarcomere
82 architecture and if the titin nano-architecture would be consistent with a ruler function
83 mechanically linking actin to myosin at a defined distance, as proposed for vertebrates. A first
84 step to answer these important questions is to determine the exact positions of the titin
85 homologs within the sarcomere.

86 Here, we chose the *Drosophila* indirect flight muscles to determine the precise
87 location of the two *Drosophila* homologs Sallimus (Sls) and Projectin (Proj). We selected key
88 domains at different locations within Sls and Proj, against which we raised specific
89 nanobodies (Loreau et al., 2022). We applied single and dual-colour DNA-PAINT super-
90 resolution microscopy to intact flight muscle specimens, which determined the precise
91 architecture of Sls and Proj in the flight muscle sarcomere. Interestingly, we found that Sls
92 but not Proj extends from the Z-disc to the myosin filament. The end of Sls overlaps with the
93 beginning of Proj, which further projects along the myosin filament. This staggered
94 organisation of the two *Drosophila* titin homologs may explain how high mechanical tension

95 can be stably transmitted across the sarcomere and how sarcomere length can be ruled without
96 the presence of a single protein linking the Z-disc to the M-band as observed in vertebrates.

97

98

99 **Results**

100 ***Drosophila* titin domain organisation and flight muscle isoforms**

101 *Drosophila* indirect flight muscles (called flight muscles in the remainder of the manuscript)
102 are stiff muscles that oscillate at high frequency to power flight (Dickinson, 2006; Pringle,
103 1981; Schönbauer et al., 2011). The majority of this stiffness is due to SIs in flight muscles
104 (Kulke et al., 2001). To achieve this high stiffness, a large part of the flexible spring domains
105 encoded in both titin gene homologs *sls* and *bent* (*bt*; protein named Projectin) are spliced out
106 by alternative splicing (Ayme-Southgate et al., 2005; Bullard et al., 2005; Burkart et al., 2007;
107 Spletter et al., 2015). Older work had suggested that the most prominent SIs flight muscle
108 isoform (also called Kettin) uses an alternative poly-A site terminating the protein after SIs-
109 immunoglobulin (Ig) domain 35 (Bullard et al., 2005; Burkart et al., 2007). However, more
110 recent systematic transcriptomics and splice-site annotation data from dissected flight muscles,
111 as well as expression of large genomic SIs-GFP tagged transgenes, showed that usage of this
112 early poly-A site is largely restricted to leg muscles and hardly present in flight muscles
113 (Spletter et al., 2015; 2018). To identify the most prominent SIs and Proj protein isoforms in
114 mature flight muscles, we carefully reanalysed the published transcriptomics and splice data
115 (Spletter et al., 2015; 2018). We verified that in both genes, the flexible PEVK spring
116 domains are largely spliced out in adult flight muscles, but their more C-terminally located
117 exons are present at least in some longer isoforms (Figure 1 – figure supplement 1A, B). This
118 predicts a SIs isoform containing the C-terminal five fibronectin (Fn) domains and a Proj
119 isoform containing a long stretch of Ig-Fn super-repeats and a kinase domain close to its C-
120 terminus (Figure 1 – figure supplement 1A, B).

121

122 **Sallimus and Projectin nanobodies in flight muscles**

123 In order to verify the expression and to determine the precise location of the different Sls
124 domains in adult flight muscle sarcomeres, we selected three different regions in Sls, against
125 which we recently generated nanobodies (Loreau et al., 2022): Sls-Ig13/14, Sls-Ig49/50 and
126 Sls-Ig51/Fn2, the first being relatively close to the N-terminus, the other two being close to
127 the C-terminus of the Sls flight muscle isoform (Figure 1 – figure supplement 1A). Similarly,
128 we selected two regions in Proj close to its N-terminus (Proj-Ig5-8 and Proj-Fn1/2) and two
129 regions close to its C-terminus (Proj-Ig27-Fn35 and Proj-kinase domain). The generation of
130 these nanobodies against Sls and Proj domains as well as their specificity, tested in
131 *Drosophila* embryonic and larval muscles, were documented in an accompanying manuscript
132 (Loreau et al., 2022).

133 To verify nanobody specificity in flight muscles, we stained *Drosophila* dorso-
134 longitudinal flight muscles with one nanobody together with phalloidin revealing the
135 sarcomere architecture. As expected, using scanning confocal microscopy, we found Sls-
136 Nano2 (binding Sls-Ig13/14) in a single sharp band overlapping with the sarcomeric Z-disc
137 (Figure 1A, B). Interestingly, Sls-Nano39 (recognising Sls-Ig49/50), Sls-Nano42 and Sls-
138 Nano48 (the latter two binding to SlsIg51/52) result in slightly broader bands at the Z-discs
139 (Figure 1B). These data further support that the Sls nanobodies are specific and they
140 demonstrate that the Sls C-terminal epitopes are indeed expressed in flight muscles, as
141 predicted from the splicing data.

142 Similarly, we investigated the nanobodies raised against the four different Projectin
143 domains. We found that Proj-Nano30 (recognising Proj-Ig5-8 very close to the N-term of
144 Proj), Proj-Nano28 and Proj-Nano29 (both binding Proj-Fn1-2) each result in a broad band at
145 the Z-disc (Figure 1C, D, Figure 1 – figure supplement 1C). Furthermore, we found that the
146 C-terminally located Proj-Nano33 (binding Proj-Ig27-Fn35) and Proj-Nano34, Proj-Nano35,

147 Proj-Nano37 and Proj-Nano46 (all binding the Projectin kinase domain) result in two bands at
148 large distances from the Z-disc (Figure 1C, D, Figure 1 – figure supplement 1C). These data
149 demonstrate that Projectin is present in an extended conformation and since the flight muscle
150 I-band extends less than 100 nm from the Z-disc (Burkart et al., 2007; Kronert et al., 2018;
151 Loison et al., 2018; Reedy and Beall, 1993; Szikora et al., 2020), a large part of Projectin is
152 present along the myosin filament. However, the diffraction-limited spatial resolution of a
153 confocal microscope is not sufficient to precisely localise SIs and Proj domains close to the Z-
154 disc. Hence, higher spatial resolution is necessary to determine the precise architecture of SIs
155 and Proj within the flight muscle sarcomere.

156

157 **Nanobodies have superior penetration compared to antibodies in flight muscles**

158 Nanobodies are only 13 kDa or less than 4 nm in size (Helma et al., 2015; Pleiner et al., 2015)
159 and hence are ideal labels for two main reasons: their small size is first placing the label very
160 close to the domain of interest and second allows efficient penetration into dense structures
161 present in cells or protein complexes which enables high labelling density. This was
162 demonstrated by the superior labelling abilities of our nanobodies compared to antibodies in
163 stage 17 embryos in an accompanying manuscript (Loreau et al., 2022). As an attempt to
164 verify if this is also the case in the crowded environment of mature flight muscles, we stained
165 flight muscles with SIs-Nano2 (binding SIs-Ig13/14) and compared them to the endogenously
166 expressed M-band protein Obscurin-GFP, or to a staining with an anti-SIs antibody (anti-
167 Kettin, binding SIs-Ig16). We imaged 10 μm thick z-stacks to quantify label diffusion into the
168 thick and crowded flight muscle fibers. Because of light scattering and fundamental limits of
169 confocal imaging, intensity of endogenously expressed labels also decays with imaging depth
170 (Sarov et al., 2016). Using the same imaging conditions and same fluorophore for SIs-Nano2
171 and the combination of anti-SIs primary and secondary antibodies, we found that the SIs-
172 Nano2 intensity decay over z-depth is about 2.5-fold lower than the one of the anti-SIs

173 antibody label (Figure 2A-C, Figure 2 – figure supplement 1). This strongly suggests better
174 penetration of the nanobody into the muscle samples compared to the larger primary and
175 secondary antibodies.

176 To directly compare the diffusion of the differently sized labels in the same samples,
177 we double-stained flight muscles with SIs-Nano2 and the SIs antibody. We swapped the dye
178 colours to rule out any bias of the excitation wavelength on penetration depth. We found that
179 SIs-Nano2 readily diffuses into the thick flight muscle samples, whereas the SIs antibody is
180 limited to the top layer of myofibrils (Figure 2 – figure supplement 2A, B). This demonstrates
181 the favourable diffusion properties of the small nanobodies in the crowded environment of
182 adult flight muscles. Labelling of myofibrils in the past was often achieved on isolated
183 myofibrils to improve antibody accessibility (Burkart et al., 2007; Szikora et al., 2020), but
184 myofibril isolation may change sarcomere mechanics and thus lead to unwanted mechanical
185 or structural artefacts (Ayme-Southgate et al., 2004; Kulke et al., 2001). The properties of
186 nanobodies make us confident that direct labelling of intact flight muscle fibers will lead to
187 dense labelling with limited structural artefacts.

188

189 **DNA PAINT super-resolution imaging of entire flight muscles**

190 In order to make use of the small size of the nanobodies, we turned our attention to super-
191 resolution imaging with DNA-PAINT (Jungmann et al., 2014; Lelek et al.; Schnitzbauer et al.,
192 2017). For DNA-PAINT, nanobodies binding the protein epitope of interest are site-
193 specifically conjugated to either one or two single-stranded DNA molecules (see Methods). In
194 DNA-PAINT, the necessary target blinking for localisation-based super-resolution
195 reconstruction is achieved by the transient binding of dye-labelled DNA ‘imager’ strands to
196 their target-bound complements (‘docking’ strands, Figure 3A). As imager strands are
197 continuously replenished from solution and binding times are controllable over a wide range,

198 a large number of photons can be detected from a single binding event, thus enabling
199 unprecedented sub-5 nm spatial resolutions (Dai et al., 2016; Schnitzbauer et al., 2017).

200 Previously, DNA-oligos for PAINT were either coupled to antibodies via biotin-
201 streptavidin (Jungmann et al., 2014), which is a 66 kDa tetramer and thus relatively large or
202 more frequently by click chemistry (Fabricius et al., 2018; Schnitzbauer et al., 2017), which
203 comes with a number of potential disadvantages, such as a bulky hydrophobic coupling group
204 and an initial lysine modification that might destroy the paratope. Instead, we used
205 maleimide-coupling through cysteines at the N- and C-terminus of the nanobody, which
206 allows a simpler workflow, analogous to direct fluorophore coupling, and protects the
207 antigen-binding site from undesired modifications.

208 In contrast to fluorophore-maleimides, maleimide-activated oligonucleotides are not
209 commercially available. However, as described in the Methods, they are straightforward to
210 synthesise from a 5' amino-modified oligo and a bifunctional maleimide-NHS (N-
211 hydroxysuccinimide) crosslinker. The NHS group forms an amide bond with the 5' amino
212 group of the oligo under reaction conditions that leave the amino groups of the DNA bases
213 non-reactive. The maleimide-activated oligo is then reacted with the nanobody that still
214 contains its His14-SUMO or His14-NEDD8 tag. The resulting conjugate is purified by
215 binding to a Ni(II) chelate matrix (whereby the non-conjugated excess of oligo remains in the
216 non-bound fraction) and followed by elution of nanobody-oligo conjugate with a tag-cleaving
217 protease. Hence, these oligo-coupled nanobodies remain similarly small as the fluorescently
218 coupled nanobodies and are thus ideal for effective super-resolution imaging using DNA-
219 PAINT.

220 We aimed to apply DNA-PAINT to flight muscle tissue, using hemi-thoraces of adult
221 flies, to minimise artefacts that might be introduced by cutting out individual myofibrils. To
222 prepare hemi-thoraces, we fixed thoraces in paraformaldehyde and then bisected them with a
223 sharp microtome knife (Figure 3 – figure supplement 1A, see Methods for details). Then, we

224 incubated the hemi-thoraces with oligo-coupled nanobodies and mounted them for imaging.
225 Hemi-thoraces are very large, with a length of about 1 mm and a thickness of about 300 μm .
226 To mount them as close as possible to the coverslip, we developed an imaging chamber that
227 contains the imaging buffer surrounded by spacers thick enough to slightly press the flight
228 muscles against the coverslip (Figure 3 – figure supplement 1A, see Methods for details). This
229 enabled DNA-PAINT imaging with total internal reflection (TIRF). We imaged for 30 min
230 per sample and obtained about 15000 frames at an imaging rate of 10 Hz. For image
231 reconstruction and post-processing, we used the established Picasso software (Schnitzbauer et
232 al., 2017) (Figure 3B, Figure 3 – figure supplement 1B, see Methods for details). This enabled
233 us to resolve the two bands flanking a Z-disc with ease, which cannot be resolved in the
234 diffraction-limited image (Figure 3B).

235 To further refine the precision of determining the epitope positions, we have
236 developed an image processing pipeline that relies on an interactive selection of well-stained
237 myofibrils in the volume of TIRF excitation (Figure 3 – figure supplement 2). Next, we
238 removed localisations arising from multiple binding events by filtering based on specific
239 localisation parameters (see Methods for details). Further, we automatically detected the
240 individual sarcomeric Z-discs and the respective flanking bands of the stained SIs or Proj
241 epitopes for all selected myofibrils. We applied a Gaussian fit to each band and determined
242 their center positions within the sarcomere with nanometric accuracy (Figure 3C, Figure 3 –
243 figure supplement 2). This results in an accurate location of the measured bands for each of
244 the epitopes in every analysed sarcomere. Hence, we do not need to average across many
245 sarcomeres to precisely localise the SIs or Proj epitopes (Figure 3C). In conclusion, our
246 method allows detecting individual differences in sarcomeric band positions in each
247 sarcomere investigated down to the nanometer-scale.

248

249 **Positions of Sallimus and Projectin domains within intact flight muscle at the**
250 **nanometric scale**

251 We applied our DNA-PAINT imaging pipeline of flight muscles to the SIs and Proj nanobody
252 toolbox. In most cases, we co-stained with two nanobodies that are spaced sufficiently apart
253 to detect the expected four bands centred around the Z-disc, even when using only a single
254 imaging colour (Figure 4). This allowed us to resolve the positions of SIs-Nano2 (SIs-Ig13/14)
255 located close to the N-terminus of Sallimus or SIs-Nano39 (SIs-Ig49/50) close to its C-
256 terminus, which we could combine with distantly located Proj nanobodies (Figure 4A).
257 Similarly, we imaged the N-terminally located Proj-Nano29 (Proj-Fn1/2) and Proj-Nano30
258 (Proj-Ig5-8), which we could combine with one of the C-terminally located Proj-Nano33
259 (Ig27-Fn35), Proj-Nano35 or Proj-Nano37 (both Proj kinase domain). This enabled us to
260 locate the exact position of different Projectin domains in sarcomeres (Figure 4A).
261 Interestingly, all the analysed epitopes result in similarly sharp bands in each of the
262 sarcomeres, suggesting a very precise linear architecture of SIs and Proj. The N-terminus of
263 SIs is located close to the Z-disc, with Ig13/14 only about 50 nm away from the center of the
264 Z-disc, whereas the N-terminus of Proj is located around 100 nm away from the Z-disc (Proj-
265 Ig5-8 and Proj-Fn1/2) and hence cannot be anchored directly at the Z-disc.

266 This single-colour imaging method is powerful, but it fails to resolve two epitopes into
267 distinct bands if the epitopes are located too close together to unambiguously assign each
268 blinking event to one particular nanobody. Thus, SIs-Nano2 (SIs-Ig13/14) and SIs-Nano39
269 (SIs-Ig49/50) or SIs-Nano2 (SIs-Ig13/14) and Proj-Nano28 (Proj-Fn1/2) cannot be imaged
270 together in the same sarcomere with a single colour (Figure 4B). However, quantifying the
271 exact positions of two closely located titin domains in the same sarcomere is critical as the
272 relative length of the flexible titin molecules may vary in individual sarcomeres. Hence, it
273 would be important to determine the positions of two different SIs domains in the same

274 sarcomere to unambiguously conclude about SIs length or the relative arrangement of its
275 protein domains.

276

277 **Two-colour DNA-PAINT reveals a staggered organisation of SIs and Proj**

278 To simultaneously determine the exact positions of two epitopes, we have labelled our
279 nanobodies with two different oligonucleotides and imaged them with two different imager
280 oligos in parallel to perform two-colour DNA-PAINT (see Methods). Multiplexed imaging
281 enabled us to determine the positions of SIs-Ig13/14 (using SIs-Nano2) and SIs-Ig51/Fn2
282 (using SIs-Nano42) in the same sarcomere (Figure 5A). Our results verified that SIs-Ig13/14
283 is localised about 50 nm away from the center of the Z-disc and that SIs-Ig51/Fn2 is about
284 50 nm further towards the middle of the sarcomere (Figure 5 – figure supplement 1). Since
285 the I-band of flight muscles is less than 100 nm from the Z-disc (Burkart et al., 2007; Kronert
286 et al., 2018; Loison et al., 2018; Reedy and Beall, 1993; Szikora et al., 2020) this strongly
287 suggests that SIs is bridging across the entire sarcomeric I-band with its N-terminus anchored
288 within the Z-disc and its C-terminal end reaching the myosin filament. Thus, SIs could
289 mechanically link the Z-disc to the myosin filament in the flight muscles, similar to the long
290 vertebrate titin.

291 Since we found that the N-terminus of Proj is also about 100 nm away from the Z-disc
292 and thus located at the beginning of the thick filament (Figure 4A) we wanted to further
293 investigate the precise orientation of the Proj N-terminal domains. We performed two-colour
294 DNA-PAINT to localise Proj-Ig5/8 (with Proj-Nano30) and Proj-Fn1/2 (with Proj-Nano29) in
295 the same sarcomere and found an average distance between the two epitopes of about 25 nm,
296 with Proj-Ig5-8 being always closer to the Z-disc relative to Proj-Fn1/2 (Figure 5B, Figure 5 –
297 figure supplement 1). Consistently, the more C-terminally located Proj-Ig27-Fn35 epitope is
298 located far into the myosin filament beginning at 100 nm (Szikora et al., 2020), being 350 nm
299 away from the Z-disc (Figure 5B, Figure 5 – figure supplement 1). This strongly suggests that

300 the N-terminal part of Proj is arranged in an extended, likely linear confirmation reaching
301 from the myosin filament into the I-band and thus running in parallel to the C-terminal
302 domains of Sls.

303 These findings raised an enticing hypothesis: do the extended Sls and Proj proteins
304 overlap at the I-band/A-band interface? To investigate this hypothesis, we performed two-
305 colour DNA-PAINT using two pairs of nanobodies: Sls-Nano39, recognising Sls-49/50,
306 combined with Proj-Nano29, binding Proj-Fn1/2 and Sls-Nano42, recognising Sls-Ig51/Fn2,
307 combined with Proj-Nano30, binding Proj-Ig5/8. Interestingly, we found that in all
308 sarcomeres measured, the Proj-Nano29 is about 15 nm further from the Z-disc than Sls-
309 Nano39, whereas in 42 out of 45 sarcomeres investigated, Proj-Nano30 is on average 7-8 nm
310 closer to the Z-disc than Sls-Nano42 (Figure 5C, Figure 5 – figure supplement 1). Hence,
311 these data revealed an interesting staggered organisation of the two overlapping ends of the
312 linearly extended Sallimus and Projectin proteins in flight muscles.

313

314 **A molecular map of the *Drosophila* titin homologs in flight muscle sarcomeres**

315 Our data enabled us to build a molecular map of the *Drosophila* titin homologs in flight
316 muscle sarcomeres, which revealed a significant overlap of the linear Sls and Proj proteins at
317 the I-band/A-band interface as visualised in a ‘composite sarcomere’ reconstructed by
318 imaging flight muscles from six different hemi-thoraces (Figure 6A).

319 To precisely determine the position of all the epitopes investigated in our study, we
320 calculated the averaged position using all the sarcomeres we imaged in the single- and dual-
321 colour DNA-PAINT experiments. This strategy is valid as we found that although our
322 mounting protocol for TIRF imaging results in a slightly variable sarcomere length around
323 3.5 μm (Spletter et al., 2015), the distance between the measured epitopes is constant (Figure
324 6 – figure supplement 1). Hence, the localisation of the Sls and Proj domains investigated
325 using all sarcomeres measured resulted in a very high localisation precision with 95%

326 confidence intervals of only 1 to 8 nm (Figure 6B). Pooling all data verified that the N-
327 terminal Proj-Ig5-8 epitope is located 90 nm from the Z-disc, whereas the C-terminal Sls
328 epitopes Sls-Ig49/50 and Sls-Ig51/Fn2 are located about 98 nm from the Z-disc. This is
329 consistent with a staggered linear organisation of Sallimus and Projectin, which suggests an
330 attractive mechanism how to mechanically link the sarcomeric Z-disc in insect flight muscle
331 with the myosin filament using both titin homologs (Figure 6C).
332

333

334 **Discussion**

335 **Super-resolution of flight muscles with nanobodies**

336 The value of nanobodies and other small binders is well appreciated (Harmansa and Affolter,
337 2018). However, most *Drosophila in vivo* studies have thus far heavily relied on
338 commercially available anti-GFP nanobodies to enhance GFP fluorescence signal in various
339 tissues, including *Drosophila* flight muscles (Kaya-Copur et al., 2021) or to either trap GFP-
340 fusion proteins ectopically or to degrade them when expressed in various modified forms *in*
341 *vivo* (Caussin et al., 2011; Harmansa et al., 2015; Nagarkar-Jaiswal et al., 2015). Our titin
342 nanobody toolbox (Loreau et al., 2022) enabled us now to apply DNA-PAINT super-
343 resolution technology to image the titin nanostructure in large intact flight muscle tissue at
344 nanometer scale resolution.

345 It had been shown that dye- or DNA-labelled nanobodies work well to achieve high
346 labelling densities in cell culture (Agasti et al., 2017; Fabricius et al., 2018; Mikhaylova et al.,
347 2015; Pleiner et al., 2015; Schlichthaerle et al., 2019). We show here that our nanobodies are
348 also very efficient in penetrating into the large flight muscle fibers containing highly packed
349 sarcomeres, which are amongst the most protein dense macromolecular structures in biology
350 (Daneshparvar et al., 2020; Taylor et al., 2019). This enabled us to perform DNA-PAINT
351 super-resolution microscopy of the large flight muscles without dissecting individual
352 myofibrils. Such large specimen have rarely been investigated with DNA-PAINT (Cheng et
353 al., 2021; Lelek et al. 2021). This shows that DNA-PAINT can be readily applied to super-
354 resolve structures in large tissues if mounting and labelling protocols are optimised.

355

356 **Titin nanoarchitecture in flight muscles – do titins rule?**

357 Flight muscles are an ideal tissue to perform architectural studies of their sarcomeric
358 components at the nanoscale, because these components display an extremely high molecular

359 order (Loison et al., 2018). This was impressively demonstrated by substructural averaging
360 that resolved the nanostructure of myosin filaments isolated from insect flight muscles at a 7Å
361 resolution by cryo-electron-microscopy (Daneshparvar et al., 2020; Hu et al., 2016). Another
362 recent study took advantage of this stereotypic order and used a series of existing antibodies
363 against sarcomeric protein components to probe isolated myofibrils from *Drosophila* flight
364 muscles using STORM (Rust et al., 2006). The high order enabled averaging of several
365 hundred sarcomeres to reconstruct distances of the epitopes from the Z-disc with 5-10 nm
366 precision (Szikora et al., 2020). Although done on isolated myofibrils, the large diversity of
367 antibodies studied gave a comprehensive understanding of domain positions for a variety of
368 important sarcomeric components. This included the Sls-Ig16 antibody used here, locating
369 Sls-Ig16 about 50 nm from the center of the Z-disc (Szikora et al., 2020), which is in good
370 agreement with the location of Sls-Ig13/14 we found here. This study further showed that the
371 important Z-disc components alpha-Actinin, Zasp52 and Filamin extend only about 35 nm
372 from the center of the Z-disc (Szikora et al., 2020). This strongly suggests that the N-terminus
373 of Sls, with its remaining 12 Ig domains can reach and interact with these Z-disc components,
374 as has been reported biochemically (González-Morales et al., 2017; Liao et al., 2016). Hence
375 the N-terminal part of the fly titin homolog Sls is arranged similarly to the N-terminus of
376 vertebrate titin that binds to alpha-Actinin, anchoring it within the Z-disc (Gautel and
377 Djinović-Carugo, 2016; Ribeiro et al., 2014).

378 An important part of the titin ruler model is that the titin spring part, which relaxes and
379 stretches during muscle contraction and relaxation, respectively, spans across the I-band and
380 sets the I-band length of vertebrate sarcomeres (Brynnel et al., 2018; Linke, 2018; Luis and
381 Schnorrer, 2021). Thus, it is insightful that our newly developed C-terminal Sls nanobodies
382 show that the C-terminal end of Sls is located about 100 nm from the center of the Z-disc in
383 flight muscles. Although we have not imaged myosin directly in our samples, both STORM
384 and electron-microscopy studies demonstrated that the myosin filament begins about 100 nm

385 from the center of the Z-disc, making the I-band less than 100 nm wide (Burkart et al., 2007;
386 Kronert et al., 2018; Loison et al., 2018; Reedy and Beall, 1993; Szikora et al., 2020). This
387 strongly suggests that, as in vertebrates, SIs is indeed spanning across the short flight muscle
388 I-band, where it could interact with its C-terminal fibronectin domains with the myosin
389 filament and hence could mechanically link the Z-disc with the myosin filament. This would
390 be consistent with SIs functioning as a I-band ruler in insect muscles (see model in Figure 6C).
391 This interpretation is also supported by the observation that non flight muscles like leg, jump
392 and larval muscles, which contain long I-bands, do express longer versions of SIs that include
393 the large and flexible PEVK domains (see Figure 1 Supplement 2A) (Burkart et al., 2007;
394 Spletter et al., 2015). Indeed, in the accompanying paper using the SIs nanobodies, we
395 showed that SIs is more than 2 μm long in larval muscles to bridge over these long I-bands
396 (Loreau et al., 2022). This strongly suggests that SIs determines I-band length in the different
397 muscle types, however, a direct genetic test that modifies SIs length and assays I-band length
398 remains to be done.

399 The vertebrate A-band contains the Ig-Fn super-repeats of titin, which extend from the
400 beginning myosin filament until the M-band, where titin's C-terminal kinase is located
401 (Granzier et al., 2014; Lange et al., 2005; Linke, 2018). Interestingly, we demonstrate that in
402 *Drosophila* flight muscles Projectin, which is very similar to the A-band part of vertebrate
403 titin, with long Ig-Fn super-repeats and a C-terminal kinase domain, starts about 90 nm from
404 the Z-disc. Hence, it is very unlikely that it can interact with Z-disc components directly as
405 these are far from the N-terminal end of Projectin (model in Figure 6C). Our precise distance
406 measurements suggest that the N-terminus of Projectin, which does contain a series of Ig
407 domains, typical for the I-band part of titin, is sticking into the flight muscle I-band, whereas
408 its first Fn/Ig super-repeat is located at beginning of the A-band (110 nm from the Z-disc) and
409 hence can interact with myosin, as can its remaining Ig-Fn super-repeats that extend over a
410 length of about 250 nm towards the M-band. The Proj kinase localises in a sharp band,

411 however it remains far from the M-band. Hence, it is hard to imagine that Proj alone can
412 directly rule A-band length of flight muscle sarcomeres, as it is only present at its distal ends,
413 spanning about 15% of the myosin filament.

414

415 **Staggering insect titins to effectively transduce forces during flight?**

416 *Drosophila* flight muscles are very stiff to effectively power wing oscillations during flight at
417 200 Hz. The perpendicular arrangement of the antagonistic dorso-ventral (DVMs) versus the
418 dorso-longitudinal flight muscles (DLMs) enables an effective stretch-activation mechanism
419 as trigger: contraction of the DVMs moves the wings up and stretches the DLMs to induce
420 their contraction, which will move the wings down again for the next cycle (Dickinson et al.,
421 2005; Pringle, 1981; Syme and JOSEPHSON, 2002). The importance of strain in these
422 muscles is highlighted by their expression of a particular troponin C isoform (TpnC4), which
423 requires to be stretched to displace tropomyosin from myosin binding sites on actin filaments
424 (Agianian et al., 2004). Furthermore, myosin also experiences a stretch-induced deformation
425 before effective actin binding and maximum force production (Iwamoto and Yagi, 2013).
426 This strongly suggests that a very effective force transmission is needed during flight muscle
427 oscillations.

428 *Drosophila* sarcomeres have a peak to peak amplitude of about 3.5 % or 60 nm per
429 half sarcomere during flight (measured in *Drosophila virilis* (Chan and Dickinson, 1996)).
430 This 3.5 % strain is needed to produce the up to 110 W/kg power output of insect flight
431 muscles (Chan and Dickinson, 1996), which is consistent with the hypothesis that strain
432 across molecules stores the elastic energy for the next contraction cycle in *Drosophila*
433 (Dickinson et al., 2005). A perfect candidate for such a molecule is SIs as it bridges across the
434 I-band, which likely changes length during the fast contraction cycles. Thus, SIs length would
435 oscillate during flight, which likely results in high oscillating forces across SIs during flight.

436 A similar storage of elastic energy has been suggested for mammalian titin during sarcomere
437 contraction cycles (Eckels et al., 2019; Rivas-Pardo et al., 2020).

438 What is the role of Projectin? The precise linear arrangement of Proj at the beginning
439 of the myosin filament and the found overlap with SIs suggests that this staggered architecture
440 of SIs and Proj might be required to effectively anchor SIs to the myosin filament and to
441 prevent sarcomere rupturing during flight. Such flight induced muscle ruptures are generated
442 when muscle attachment to tendons is weakened, underscoring the high muscle forces and
443 high strain produced during flight (Lemke et al., 2019). Projectin may thus serve as an
444 effective glue to stably connect SIs to the myosin filament. This is also consistent with the
445 findings that both SIs and Proj are needed to assembly contractile sarcomeres in *Drosophila*
446 larval muscles. Knock-down of each of the proteins results in embryonic lethality and
447 defective sarcomerogenesis (Loreau et al., 2022; Schnorrer et al., 2010). Taken together, the
448 staggered architecture of the two *Drosophila* titin homologs may effectively allow force
449 transduction and ensure mechanical integrity of flight muscles sarcomeres, both very
450 prominent functions of mammalian titin (Li et al., 2020; Rivas-Pardo et al., 2020; Swist et al.,
451 2020).

452

453 **Methods**

454 *Fly strains and fly culture*

455 Fly stocks were grown and maintained under normal culture conditions in humidified
456 incubators with 12-hour light-dark cycles on standard fly medium (Avellaneda et al., 2021).
457 The particularly well flying ‘Luminy’ strain was used in all experiments as wild type (Leonte
458 et al., 2021). The Obscurin-GFP strain contains a large genomic clone expressing Obscurin
459 (unc-89) tagged with GFP at its C-terminus (Sarov et al., 2016). For all experiments young 3
460 to 10 day old flies were used.

461

462 *Nanobody production and labelling*

463 Nanobody production and labelling with fluorophores by maleimide chemistry through
464 ectopic cysteines was done as described in detail in the accompanying paper (Loreau et al.,
465 2022). To couple nanobodies to DNA oligos, the oligos (P1, P2, PS3) were ordered with a 5'
466 amino group modification (e.g., Am-C6-TTT CTT CAT TAC) from IBA (Göttingen) in
467 HPLC-purified form and lyophilized as a three ethyl ammonium (TEA) salt. Note that the
468 absence of ammonia (NH_4^+) is essential for the procedure. 1 μmol of oligo was dissolved in
469 200 μl 30% acetonitrile (ACN), 15 mM TEA, which yielded a 5 mM stock at neutral pH (~ 7).
470 5 μl of a 100 mM crosslinker stock in 100% ACN (maleimido β -alanine NHS ester, Iris
471 Biotec # MAA1020 or mal-PEG4-NHS, Iris Biotec # PEG1575) were added and allowed to
472 react for 30 minutes on ice. Then, 1.6 μl 5 M sodium acetate, and 0.1 M acetic acid (pH ~ 7)
473 were added, and the modified oligo was precipitated by adding 1 ml 100% ACN and
474 centrifugation for 10 minutes at 0°C at 12000 rpm. This step removes any non-reacted
475 maleimide. The pellet was then dissolved in 100 μl 30% ACN, and either stored in small
476 aliquots at -80°C or used directly to label nanobodies at ectopic, reduced cysteines, as
477 described for fluorophores in the accompanying paper (Loreau et al., 2022). Note that free
478 oligo cannot be removed by gelfiltration on Sephadex G25 because it appears with the

479 conjugate in the void volume. It is best removed by modifying a still His14-SUMO, or His14-
480 NEDD8 tagged nanobody and then using Ni(II) capture (where the free oligo remains non-
481 bound) and proteolytic release of the then tag-free nanobody conjugate. The efficiency of
482 conjugation can be assessed by SDS-PAGE, in which the oligo-modification results in a clear
483 size shift. In addition, the density of modification can be calculated through OD260 and
484 OD280 readings, using ϵ_{260} and ϵ_{280} of the initial oligo and nanobody as input variables.
485 The oligo modification by this method is usually quantitative already with a small (≥ 1.1)
486 molar excess of the maleimide oligo over modifiable cysteines. In case of incomplete
487 modification, the conjugate can be purified on a MonoQ column, whereby the highly negative
488 charged oligo causes stronger retention of the conjugate as compared to the non-modified
489 nanobody.

490

491 *Flight muscle preparation, staining and mounting for imaging*

492 Intact hemi-thoraces from adult males were prepared similar as described (Weitkunat and
493 Schnorrer, 2014). Head, wings and abdomen were clipped with sharp forceps and the intact
494 thoraces were fixed for 20 min at room temperature in relaxing solution (4% PFA in 100mM
495 NaCl, 20mM NaPi pH7.2, 6mM MgCl₂, 5mM ATP, 0.5% Triton X-100). After washing
496 twice with relaxing solution, the thoraces were placed on a slide with double-sticky tape and
497 cut sagittally with a sharp microtome blade (Pfm Medical Feather C35). The fixed hemi-
498 thoraces were transferred to 24-well plates or Eppendorf tubes and blocked for 30 min at
499 room temperature with 3% normal goat serum in PBS + 0.5% Tx-100 (PBS-T). Hemi-
500 thoraces were stained overnight at 4°C with the combinations of nanobodies indicated,
501 labelled with fluorophores or oligonucleotides (final concentration of about 50 nM). The rat
502 anti-SIs antibody (anti-Kettin, MAC155/Klg16, Babraham Bioscience Technologies) was
503 diluted 1:1000 and visualised with fluorescently labelled secondary antibodies (ThermoFisher,
504 Molecular Probes). Actin was stained with phalloidin-rhodamine or phalloidin-Alexa488

505 (1:2000, ThermoFisher; 2 h at room temperature or overnight at 4°C). To mount the flight
506 muscles as close as possible to the coverslip, an imaging chamber was build using a slide and
507 #1 coverslips as spacers right and left of the samples. A layer of double sticky tape was built
508 on the spacer and the imaging chamber was filled with either SlowFade™ Gold Antifade
509 (Thermofisher) for confocal imaging or Imager solution for DNA-PAINT imaging. Stained
510 hemi-thoraces were added, oriented with the flight muscles facing up and #1.5 coverslip was
511 added. The chamber was sealed with nail polish for confocal imaging or Picodent glue for
512 DNA-PAINT imaging.

513

514 *Confocal imaging and processing*

515 Stained flight muscles were imaged on a Zeiss LSM880 confocal with a 63x oil lens. Images
516 were processed using Fiji (Schindelin et al., 2012).

517

518 *Analysing antibody versus nanobody labelling intensity decay over depth*

519 We manually drew selections with Fiji (Schindelin et al., 2012) on stacks obtained with
520 confocal imaging; each selection consisted of one myofibril. We used these selections to
521 extract intensity profiles that were then analysed automatically using Python custom codes.
522 The automated analysis to extract the intensity of each band consisted of the following: (a)
523 locate bands in profiles using the peak finding algorithm `find_peaks` from the `scipy` library; (b)
524 subtract background on the profile, linear fitting the 35% lowest values of the profile and
525 subtracting this fit on the profile; (c) fit bands on the background-corrected profile with
526 Gaussian functions; (d) estimate the area under the curve of these fits. This initial analysis
527 allowed us to estimate the integrated intensity of bands of Obscurin-GFP and epitopes
528 labelled with Sls-Ig16 antibody and Sls-Ig13/14 nanobody. In order to estimate how fast
529 intensity decays with depth when imaging these bands with confocal microscopy, for each
530 animal we fitted with an exponential decay function to the averaged band intensity over each

531 selection (a myofibril) versus the depth where it was imaged (Figure 2 – figure supplement 1).
532 The decay lengths obtained were then reported in Figure 2C. In our imaging conditions, the
533 decay of intensity with depth of GFP was higher than the one of SIs-Nano2, likely caused by
534 faster bleaching of GFP compared to the Alexa488 dye when acquiring a z-stack.

535

536 *DNA-PAINT imaging*

537 Materials: Cy3B-modified and Atto643-modified DNA oligonucleotides were custom-ordered
538 from Metabion. Sodium chloride 5 M (cat: AM9759) was obtained from Ambion. Coverslips
539 (cat: 0107032) and glass slides (cat: 10756991) were purchased from Marienfeld and Thermo
540 Fisher. Double-sided tape (cat: 665D) was ordered from Scotch. Two component silica twinstil
541 speed 22 (cat. 1300 1002) was ordered from picodent. Glycerol (cat: 65516-500ml), methanol
542 (cat: 32213-2.5L), protocatechuate 3,4-dioxygenase pseudomonas (PCD) (cat: P8279), 3,4-
543 dihydroxybenzoic acid (PCA) (cat: 37580-25G-F) and (+/-)-6-hydroxy-2,5,7,8- tetra-
544 methylchromane-2-carboxylic acid (Trolox) (cat: 238813-5 G) were ordered from Sigma.
545 Potassium chloride (cat: 6781.1) was ordered from Carl Roth. Paraformaldehyde (cat: 15710)
546 were obtained from Electron Microscopy Sciences. 90 nm diameter Gold Nanoparticles (cat:
547 G-90-100) were ordered from cytodiagnosics.

548 Buffers: For imaging the following buffer was prepared: Buffer C (1× PBS, 500 mM NaCl).
549 Directly before imaging Buffer C was supplemented with: 1× Trolox, 1× PCA and 1× PCD
550 (see paragraph below for details). 100x Trolox: 100 mg Trolox, 430 µl 100 % Methanol,
551 345 µl 1M NaOH in 3.2 ml H₂O. 40× PCA: 154 mg PCA, 10 ml water and NaOH were mixed,
552 and pH was adjusted 9.0. 100× PCD: 9.3 mg PCD, 13.3 ml of buffer (100 mM Tris-HCl pH 8,
553 50 mM KCl, 1 mM EDTA, 50 % Glycerol). All three were frozen and stored at -20 °C.

554 Sample preparation. *Drosophila* hemi-thoraces were isolated and stained as described above
555 with phalloidin Alexa488 (1:2000) and the two nanobodies coupled to either P1, P3 or PS3
556 oligos (about 50 nM) overnight. Before embedding the samples into the chamber, they were

557 washed two times with PBS + 1% Triton. Hemi-thoraces were embedded as described above.
 558 Before assembling the chamber, the cover slip was treated with 90 nm diameter gold
 559 nanoparticles (cat: G-90-100, Cytodiagnostics, 1:10 dilution into methanol). After assembling,
 560 the chamber was filled with imaging buffer containing the complementary P1, P3 or PS3
 561 imaging oligos (see below for imaging conditions) and sealed with Picodent glue.

562 Super-resolution microscope: Fluorescence imaging was carried out on an inverted
 563 microscope (Nikon Instruments, Eclipse Ti2) with the Perfect Focus System, applying an
 564 objective-type TIRF configuration with an oil-immersion objective (Nikon Instruments, Apo
 565 SR TIRF 100x, NA 1.49, Oil). A 561 nm and 640 nm (MPB Communications Inc., 2 W,
 566 DPSS-system) laser were used for excitation. The laser beam was passed through clean-up
 567 filters (Chroma Technology, ZET561/10, ZET642/20x) and coupled into the microscope
 568 objective using a beam splitter (Chroma Technology, ZT561rdc, ZT647rdc). Fluorescence
 569 light was spectrally filtered with an emission filter (Chroma Technology, ET600/50m and
 570 ET575lp, ET705/72m and ET665lp) and imaged on a sCMOS camera (Andor, Zyla 4.2 Plus)
 571 without further magnification, resulting in an effective pixel size of 130 nm (after 2×2
 572 binning).

573 Imaging conditions:

574 *Figure 4*

Sample	Nb inner	Nb outer	Power	Imager	Exposure	# Frames	Dye
5	Nano2	Nano35	58 mW	P3 2 nM	100 ms	15000	Cy3B
4	Nano2	Nano33	58 mW	P3 2 nM	100 ms	15000	Cy3B
17	Nano39	Nano35	58 mW	P3 2 nM	100 ms	15000	Cy3B
9	Nano29	Nano33	58 mW	P3 2 nM	100 ms	15000	Cy3B
11	Nano29	Nano37	58 mW	P3 2 nM	100 ms	15000	Cy3B
13	Nano30	Nano33	58 mW	P3 2 nM	100 ms	15000	Cy3B
15	Nano30	Nano37	58 mW	P3 2 nM	100 ms	15000	Cy3B
1	Nano2	Nano28	58 mW	P3 2 nM	100 ms	15000	Cy3B
7	Nano2	Nano39	58 mW	P3 2 nM	100 ms	15000	Cy3B

575

576 *Figure 5*

Sample	Nanobody	Power	Imager	Exposure	# Frames	Dye
1	Nano 42	50 mW	P1 2 nM	100 ms	15000	Atto643
1	Nano 2	50 mW	P3 2 nM	100 ms	15000	Cy3B
6	Nano 29	50 mW	P1 2 nM	100 ms	15000	Atto643
6	Nano 30	50 mW	P3 2 nM	100 ms	15000	Cy3B
7	Nano 29	50 mW	P1 2 nM	100 ms	15000	Atto643

7	Nano 33	50 mW	P ₃ 2 nM	100 ms	15000	Cy3B
9	Nano 29	50 mW	PS ₃ 2 nM	100 ms	15000	Atto643
9	Nano 99	50 mW	P ₃ 2 nM	100 ms	15000	Cy3B
14	Nano 42	50 mW	P ₁ 2 nM	100 ms	15000	Atto643
14	Nano 30	50 mW	P ₃ 2 nM	100 ms	15000	Cy3B

577

Name	Imager	Docking site
P1 – Atto643	TAGATGTAT – Atto643	Nanobody - TTATACATCTA
P3 – Cy3b	TAATGAAGA – Cy3B	Nanobody - TTTCTTCATTA
PS3 – Atto643	TCCTCCC – Atto643	Nanobody - AAGGGAGGA

578

579

580 Super-resolved image reconstruction: The data acquired during imaging was post-processed
581 using the Picasso (Schnitzbauer et al., 2017) pipeline. First, the localisations were detected by
582 a threshold-based detection and fitted with a least-square fit. Next, the data was drift corrected
583 using a redundant cross-correlation and a fiducial marker-based drift correction. Then, a
584 super-resolved image was rendered using Picasso render. From the images, the myofibrils for
585 further analysis were selected interactively using the rectangular pick tool. All further analysis
586 was done with customized jupyter notebooks.

587

588 *Extraction of band positions from DNA-PAINT data*

589 Extraction of band positions from DNA-PAINT data was achieved the following way: first,
590 individual myofibrils were manually selected using the rectangular selection tool from
591 Picasso (Schnitzbauer et al., 2017) and saved in individual files.

592 Second, the remaining of the analysis was automated in custom codes written in
593 Python. To limit localisation events arising from multiple emitters that create artefacts (Lelek
594 et al. 2021), localisations were filtered based on the standard deviation of their Gaussian fits.
595 Localisations kept were within a disc in the standard deviation space (sx, sy), centered on the
596 maximum of the distribution and of radius 0.2 pixel.

597 Third, individual Z-discs were automatically detected. This did not require super-
598 resolved data and the process was the result of multiple steps: (a) the algorithm rotated
599 selections and their localisations to orient the selection horizontally. (b) Localisations were
600 projected along the main axis of the selection and their density was reported in a histogram,

601 which bins size was the same as the pixel size of the camera. The histogram can be seen as a
602 low resolution intensity profile along the myofibril. (c) The algorithm found peaks in the
603 resulting histogram (with `find_peaks` from the `scipy` library) corresponding to positions of Z-
604 discs. (d) Once peaks were detected, the algorithm selected peaks that were relevant to the
605 analysis, using the fact that the distance between Z-discs is the size of a sarcomere.

606 Fourth, with the knowledge of Z-disc positions, the algorithm then focused on windows
607 centered on Z-discs to extract the positions of bands: (a) Similar to step 3, the algorithm
608 rotated the selection and stored localisations in a histogram, which bin size is adjusted for best
609 results (typical bin size was 13 nm). (b) Because DNA-PAINT data accumulate the
610 localisations, the histogram of localisations can display fluctuations that make automated
611 extraction of band positions difficult. Therefore, to locate the rough position of a given band,
612 the data were first convolved with a Gaussian function of standard deviation 25 nm that
613 smoothens fluctuations. (c) The resulting histogram was then analysed with a peak finding
614 algorithm to locate rough band positions. (d) Finally, to precisely locate band positions, the
615 algorithm fitted a Gaussian function on the non-convolved data, in a window centered on each
616 of the positions detected at the previous step. To ensure that the analysis was properly
617 achieved, the results were visually checked.

618

619 *Averaged epitope positions using bootstrapping*

620 To obtain an uncertainty estimate of the averaged position of epitopes, we used the
621 bootstrapping method <https://doi.org/10.1007/978-1-4899-4541-9>. In brief, each dataset of an
622 epitope is used to create 1000 bootstrap replicates. We generated a replicate by drawing
623 individual values in a given dataset with replacement (*i.e.* each value can be drawn multiple
624 times). The size of one replicate is the same as the one of the initial dataset. From each of
625 these replicates we computed the mean, and therefore obtained 1000 means from 1000
626 replicates. These 1000 means constitute the bootstrap data presented in Figure 6, each epitope

627 having its own bootstrap data. Finally, 95% confidence intervals were obtained by extracting
628 the 2.5% and 97.5% quartiles from these bootstrap data.

629

630 **Acknowledgements**

631 We thank Sandra B Lemke and Aynur Kaya-Çopur for their help in the initial DNA-PAINT
632 pilot experiments. We would like to thank Stefan Raunser and Mathias Gautel and all their
633 group members as well as the Schnorrer and Görlich groups for their stimulating discussions
634 within the StuDySARCOMERE ERC synergy grant. We are indebted to the IBDM imaging
635 facility for help with image acquisition and maintenance of the microscopes.

636

637 **Funding**

638 This work was supported by the Centre National de la Recherche Scientifique (CNRS,
639 F.Schn.), the Max Planck Society (R.J., D. G.), Aix-Marseille University (P.M.), the
640 European Research Council under the European Union's Horizon 2020 Programme (ERC-
641 2019-SyG 856118 to D.G. & F.Schn. and ERC-2015-StG 680241 to R.J.), the German
642 Research Foundation through the SFB1032 (Project-ID 201269156 to R.J.), the excellence
643 initiative Aix-Marseille University A*MIDEX (ANR-11-IDEX-0001-02, F.S.), the French
644 National Research Agency with ANR-ACHN MUSCLE-FORCES (F.S.), the Human
645 Frontiers Science Program (HFSP, RGP0052/2018, F.S.), the Bettencourt Foundation (F.S.),
646 the France-BioImaging national research infrastructure (ANR-10-INBS-04-01) and the
647 Investissements d'Avenir, French Government program managed by the French National
648 Research Agency (ANR-16-CONV-0001) and from Excellence Initiative of Aix-Marseille
649 University - A*MIDEX (Turing Center for Living Systems).

650

651 The funders had no role in study design, data collection and analysis, decision to publish, or
652 preparation of the manuscript.

653

654 **Competing interests**

655 The authors declare no competing interests.

656 **References**

657 Agasti, S.S., Wang, Y., Schueder, F., Sukumar, A., Jungmann, R., and Yin, P. (2017). DNA-barcoded
658 labeling probes for highly multiplexed Exchange-PAINT imaging. *Chem Sci* 8, 3080–3091.

659 Agianian, B., Kržič, U., Qiu, F., Linke, W.A., Leonard, K., and Bullard, B. (2004). A troponin switch
660 that regulates muscle contraction by stretch instead of calcium. *The EMBO Journal* 23, 772–779.

661 Avellaneda, J., Rodier, C., Daian, F., Brouilly, N., Rival, T., Luis, N.M., and Schnorrer, F. (2021).
662 Myofibril and mitochondria morphogenesis are coordinated by a mechanical feedback mechanism in
663 muscle. *Nature Communications* 12, 2091–18.

664 Ayme-Southgate, A., Bounaix, C., Riebe, T.E., and Southgate, R. (2004). Assembly of the giant
665 protein projectin during myofibrillogenesis in *Drosophila* indirect flight muscles. *BMC Cell Biol.* 5,
666 17.

667 Ayme-Southgate, A., Saide, J., Southgate, R., Bounaix, C., Cammarato, A., Patel, S., and Wussler, C.
668 (2005). In indirect flight muscles *Drosophila* projectin has a short PEVK domain, and its NH2-
669 terminus is embedded at the Z-band. *J Muscle Res Cell Motil* 26, 467–477.

670 Brynnel, A., Hernandez, Y., Kiss, B., Lindqvist, J., Adler, M., Kolb, J., van der Pijl, R., Gohlke, J.,
671 Strom, J., Smith, J., et al. (2018). Downsizing the molecular spring of the giant protein titin reveals
672 that skeletal muscle titin determines passive stiffness and drives longitudinal hypertrophy. *eLife* 7,
673 1065.

674 Bullard, B., Burkart, C., Labeit, S., and Leonard, K. (2005). The function of elastic proteins in the
675 oscillatory contraction of insect flight muscle. *J Muscle Res Cell Motil* 26, 479–485.

676 Burkart, C., Qiu, F., Brendel, S., Benes, V., Hååg, P., Labeit, S., Leonard, K., and Bullard, B. (2007).
677 Modular proteins from the *Drosophila* sallimus (sls) gene and their expression in muscles with
678 different extensibility. *Journal of Molecular Biology* 367, 953–969.

679 Caussin, E., Kanca, O., and Affolter, M. (2011). Fluorescent fusion protein knockout mediated by
680 anti-GFP nanobody. *Nat. Struct. Mol. Biol.* 19, 117–121.

681 Chan, W.P., and Dickinson, M.H. (1996). In vivo length oscillations of indirect flight muscles in the
682 fruit fly *Drosophila virilis*. *J Exp Biol* 199, 2767–2774.

683 Cheng, J., Allgeyer, E.S., Richens, J.H., Džafić, E., Palandri, A., Lewkow, B., Sirinakis, G., and
684 Johnston, D.S. (2021). A method for single molecule localization microscopy of tissues reveals non-
685 random distribution of nuclear pores in *Drosophila*. *bioRxiv* 2021.05.24.445468.

686 Dai, M., Jungmann, R., and Yin, P. (2016). Optical imaging of individual biomolecules in densely
687 packed clusters. *Nature Nanotechnology* 11, 798–807.

688 Daneshparvar, N., Taylor, D.W., O’Leary, T.S., Rahmani, H., Abbasiyeganeh, F., Previs, M.J., and
689 Taylor, K.A. (2020). CryoEM structure of *Drosophila* flight muscle thick filaments at 7 Å resolution.
690 *Life Sci. Alliance* 3.

691 Dickinson, M. (2006). Insect flight. *Current Biology* 16, R309–R314.

- 692 Dickinson, M., Bekyarova, T., Gore, D., and Maughan, D. (2005). Molecular dynamics of cyclically
693 contracting insect flight muscle in vivo. *Nature* 433, 330–334.
- 694 Eckels, E.C., Haldar, S., Tapia-Rojo, R., Rivas-Pardo, J.A., and Fernandez, J.M. (2019). The
695 Mechanical Power of Titin Folding. *CellReports* 27, 1836–1847.e4.
- 696 Ehler, E., and Gautel, M. (2008). The sarcomere and sarcomerogenesis. *Adv. Exp. Med. Biol.* 642, 1–
697 14.
- 698 Fabricius, V., Lefèbre, J., Geertsema, H., Marino, S., Ewers, H. (2018). Rapid and efficient C-terminal
699 labeling of nanobodies for DNA-PAINT. *Journal of Physics D: Applied Physics*.
- 700 Gautel, M. (2011). The sarcomeric cytoskeleton: who picks up the strain? *Current Opinion in Cell*
701 *Biology* 23, 39–46.
- 702 Gautel, M., and Djinić-Carugo, K. (2016). The sarcomeric cytoskeleton: from molecules to motion.
703 *Journal of Experimental Biology* 219, 135–145.
- 704 González-Morales, N., Holenka, T.K., and Schöck, F. (2017). Filamin actin-binding and titin-binding
705 fulfill distinct functions in Z-disc cohesion. *PLoS Genetics* 13, e1006880.
- 706 Granzier, H.L., Hutchinson, K.R., Tonino, P., Methawasin, M., Li, F.W., Slater, R.E., Bull, M.M.,
707 Saripalli, C., Pappas, C.T., Gregorio, C.C., et al. (2014). Deleting titin's I-band/A-band junction
708 reveals critical roles for titin in biomechanical sensing and cardiac function. *Proceedings of the*
709 *National Academy of Sciences* 111, 14589–14594.
- 710 Harmansa, S., and Affolter, M. (2018). Protein binders and their applications in developmental
711 biology. *Development* 145.
- 712 Harmansa, S., Hamaratoglu, F., Affolter, M., and Caussinus, E. (2015). Dpp spreading is required for
713 medial but not for lateral wing disc growth. *Nature* 527, 317–322.
- 714 Helma, J., Cardoso, M.C., Muyldermans, S., and Leonhardt, H. (2015). Nanobodies and recombinant
715 binders in cell biology. *The Journal of Cell Biology* 209, 633–644.
- 716 Hu, Z., Taylor, D.W., Reedy, M.K., Edwards, R.J., and Taylor, K.A. (2016). Structure of myosin
717 filaments from relaxed *Lethocerus* flight muscle by cryo-EM at 6 Å resolution. *Sci Adv* 2, e1600058.
- 718 Huxley, H.E. (1969). The mechanism of muscular contraction. *Science* 164, 1356–1365.
- 719 Iwamoto, H., and Yagi, N. (2013). The molecular trigger for high-speed wing beats in a bee. *Science*
720 341, 1243–1246.
- 721 Jungmann, R., Avendaño, M.S., Woehrstein, J.B., Dai, M., Shih, W.M., and Yin, P. (2014).
722 Multiplexed 3D cellular super-resolution imaging with DNA-PAINT and Exchange-PAINT. *Nature*
723 *Methods* 11, 313–318.
- 724 Kaya-Copur, A., Marchiano, F., Hein, M.Y., Alpern, D., Russeil, J., Luis, N.M., Mann, M., Deplancke,
725 B., Habermann, B.H., and Schnorrer, F. (2021). The Hippo pathway controls myofibril assembly and
726 muscle fiber growth by regulating sarcomeric gene expression. *eLife* 10.
- 727 Kronert, W.A., Bell, K.M., Viswanathan, M.C., Melkani, G.C., Trujillo, A.S., Huang, A., Melkani, A.,
728 Cammarato, A., Swank, D.M., and Bernstein, S.I. (2018). Prolonged cross-bridge binding triggers
729 muscle dysfunction in a *Drosophila* model of myosin-based hypertrophic cardiomyopathy. *eLife* 7,
730 2446.

- 731 Kulke, M., Neagoe, C., Kolmerer, B., Minajeva, A., Hinssen, H., Bullard, B., and Linke, W.A. (2001).
732 Kettin, a major source of myofibrillar stiffness in *Drosophila* indirect flight muscle. *Journal of Cell*
733 *Biology* *154*, 1045–1057.
- 734 Lange, S., Ehler, E., and Gautel, M. (2006). From A to Z and back? Multicompartment proteins in the
735 sarcomere. *Trends in Cell Biology* *16*, 11–18.
- 736 Lange, S., Xiang, F., Yakovenko, A., Vihola, A., Hackman, P., Rostkova, E., Kristensen, J.,
737 Brandmeier, B., Franzen, G., Hedberg, B., et al. (2005). The kinase domain of titin controls muscle
738 gene expression and protein turnover. *Science* *308*, 1599–1603.
- 739 Lelek, M., Gyparaki, M.T., Beliu, G., Schueder, F., Grieffie, J., Manley, S., Jungmann, R., Sauer, M.,
740 Lakadamyali, M., Zimmer, C. (2021) Single-molecule localization microscopy. *Nature Review*
741 *Methods Primers*.
- 742 Lemke, S.B., and Schnorrer, F. (2017). Mechanical forces during muscle development. *Mechanisms*
743 *of Development* *144*, 92–101.
- 744 Lemke, S.B., Weidemann, T., Cost, A.-L., Grashoff, C., and Schnorrer, F. (2019). A small proportion
745 of Talin molecules transmit forces at developing muscle attachments in vivo. *PLoS Biol* *17*, e3000057.
- 746 Leonte, M.-B., Leonhardt, A., Borst, A., and Mauss, A.S. (2021). Aerial course stabilization is
747 impaired in motion-blind flies. *Journal of Experimental Biology*.
- 748 Li, Y., Hessel, A.L., Unger, A., Ing, D., Recker, J., Koser, F., Freundt, J.K., and Linke, W.A. (2020).
749 Graded titin cleavage progressively reduces tension and uncovers the source of A-band stability in
750 contracting muscle. *eLife* *9*.
- 751 Liao, K.A., González-Morales, N., and Schöck, F. (2016). Zasp52, a Core Z-disc Protein in
752 *Drosophila* Indirect Flight Muscles, Interacts with α -Actinin via an Extended PDZ Domain. *PLoS*
753 *Genetics* *12*, e1006400.
- 754 Linke, W.A. (2018). Titin Gene and Protein Functions in Passive and Active Muscle. *Annu. Rev.*
755 *Physiol.* *80*, 389–411.
- 756 Llewellyn, M.E., Barretto, R.P.J., Delp, S.L., and Schnitzer, M.J. (2008). Minimally invasive high-
757 speed imaging of sarcomere contractile dynamics in mice and humans. *Nature* *454*, 784–788.
- 758 Loison, O., Weitkunat, M., Kaya-Copur, A., Nascimento-Alves, C., Matzat, T., Spletter, M.L.,
759 Luschnig, S., Brasselet, S., Lenne, P.-F., and Schnorrer, F. (2018). Polarization-resolved microscopy
760 reveals a muscle myosin motor-independent mechanism of molecular actin ordering during sarcomere
761 maturation. *PLoS Biol* *16*, e2004718.
- 762 Loreau, V., Rees, R., Chan, E.H., Taxer, W., Gregor, K., Mußil, B., Pitaval, C., Luis, N.M., Mangeol,
763 P., Schnorrer, F., and Görlich, D. (2022). A nanobody toolbox to investigate localisation and dynamics
764 of *Drosophila* titins. xxx bioRxiv.
- 765 Luis, N.M., and Schnorrer, F. (2021). Mechanobiology of muscle and myofibril morphogenesis. *Cells*
766 *& Development* 203760.
- 767 Mikhaylova, M., Cloin, B.M.C., Finan, K., van den Berg, R., Teeuw, J., Kijanka, M.M., Sokolowski,
768 M., Katrukha, E.A., Maidorn, M., Opazo, F., et al. (2015). Resolving bundled microtubules using anti-
769 tubulin nanobodies. *Nature Communications* *6*, 7933–7937.
- 770 Nagarkar-Jaiswal, S., Nagarkar-Jaiswal, S., Lee, P.-T., Lee, P.-T., Campbell, M.E., Campbell, M.E.,
771 Chen, K., Anguiano-Zarate, S., Anguiano-Zarate, S., Gutierrez, M.C., et al. (2015). A library of

- 772 MiMICs allows tagging of genes and reversible, spatial and temporal knockdown of proteins in
773 *Drosophila*. *eLife* 4, 2743.
- 774 Pleiner, T., Bates, M., Trakhanov, S., Lee, C.-T., Schliep, J.E., Chug, H., Böhning, M., Stark, H.,
775 Urlaub, H., and Görlich, D. (2015). Nanobodies: site-specific labeling for super-resolution imaging,
776 rapid epitope-mapping and native protein complex isolation. *eLife* 4, e11349.
- 777 Pringle, J.W. (1981). The Bidder Lecture - The evolution of fibrillar muscle in insects. *J Exp Biol* 94,
778 1–14.
- 779 Reedy, M.C., and Beall, C. (1993). Ultrastructure of developing flight muscle in *Drosophila*. I.
780 Assembly of myofibrils. *Dev. Biol.* 160, 443–465.
- 781 Regev, G.J., Kim, C.W., Tomiya, A., Lee, Y.P., Ghofrani, H., Garfin, S.R., Lieber, R.L., and Ward,
782 S.R. (2011). Psoas Muscle Architectural Design, In Vivo Sarcomere Length Range, and Passive
783 Tensile Properties Support Its Role as a Lumbar Spine Stabilizer. *Spine* 36, E1666–E1674.
- 784 Ribeiro, E. de A., Pinotsis, N., Ghisleni, A., Salmazo, A., Konarev, P.V., Kostan, J., Sjöblom, B.,
785 Schreiner, C., Polyansky, A.A., Gkoukoulia, E.A., et al. (2014). The structure and regulation of
786 human muscle α -actinin. *Cell* 159, 1447–1460.
- 787 Rivas-Pardo, J.A., Li, Y., Mártonfalvi, Z., Tapia-Rojo, R., Unger, A., Fernández-Trasancos, Á.,
788 Herrero-Galán, E., Velázquez-Carreras, D., Fernandez, J.M., Linke, W.A., et al. (2020). A HaloTag-
789 TEV genetic cassette for mechanical phenotyping of proteins from tissues. *Nature Communications* 11,
790 2060–13.
- 791 Rust, M.J., Bates, M., and Zhuang, X. (2006). Sub-diffraction-limit imaging by stochastic optical
792 reconstruction microscopy (STORM). *Nature Methods* 3, 793–795.
- 793 Sarov, M., Barz, C., Jambor, H., Hein, M.Y., Schmied, C., Suchold, D., Stender, B., Janosch, S., K J,
794 V.V., Krishnan, R.T., et al. (2016). A genome-wide resource for the analysis of protein localisation in
795 *Drosophila*. *eLife* 5, e12068.
- 796 Schindelin, J., Arganda-Carreras, I., Frise, E., Kaynig, V., Longair, M., Pietzsch, T., Preibisch, S.,
797 Rueden, C., Saalfeld, S., Schmid, B., et al. (2012). Fiji: an open-source platform for biological-image
798 analysis. *Nature Methods* 9, 676–682.
- 799 Schlichthaerle, T., Strauss, M.T., Schueder, F., Auer, A., Nijmeijer, B., Kueblbeck, M., Jimenez
800 Sabinina, V., Thevathasan, J.V., Ries, J., Ellenberg, J., et al. (2019). Direct Visualization of Single
801 Nuclear Pore Complex Proteins Using Genetically-Encoded Probes for DNA-PAINT. *Angew. Chem.*
802 *Int. Ed. Engl.* 58, 13004–13008.
- 803 Schnitzbauer, J., Strauss, M.T., Schlichthaerle, T., Schueder, F., and Jungmann, R. (2017). Super-
804 resolution microscopy with DNA-PAINT. *Nat Protoc* 12, 1198–1228.
- 805 Schnorrer, F., Schönbauer, C., Langer, C.C.H., Dietzl, G., Novatchkova, M., Schernhuber, K., Fellner,
806 M., Azaryan, A., Radolf, M., Stark, A., et al. (2010). Systematic genetic analysis of muscle
807 morphogenesis and function in *Drosophila*. *Nature* 464, 287–291.
- 808 Schönbauer, C., Distler, J., Jährling, N., Radolf, M., Dodt, H.-U., Frasch, M., and Schnorrer, F. (2011).
809 Spalt mediates an evolutionarily conserved switch to fibrillar muscle fate in insects. *Nature* 479, 406–
810 409.
- 811 Spletter, M.L., Barz, C., Yeroslaviz, A., Schönbauer, C., Ferreira, I.R.S., Sarov, M., Gerlach, D., Stark,
812 A., Habermann, B.H., and Schnorrer, F. (2015). The RNA-binding protein Arrest (Bruno) regulates
813 alternative splicing to enable myofibril maturation in *Drosophila* flight muscle. *EMBO Rep* 16, 178–
814 191.

- 815 Spletter, M.L., Barz, C., Yeroslaviz, A., Zhang, X., Lemke, S.B., Bonnard, A., Brunner, E., Cardone,
816 G., Basler, K., Habermann, B.H., et al. (2018). A transcriptomics resource reveals a transcriptional
817 transition during ordered sarcomere morphogenesis in flight muscle. *eLife* 7, 1361.
- 818 Squire, J.M., Al-Khayat, H.A., Knupp, C., and Luther, P.K. (2005). Molecular architecture in muscle
819 contractile assemblies. *Adv Protein Chem* 71, 17–87.
- 820 Swist, S., Unger, A., Li, Y., Vöge, A., Frieling-Salewsky, Von, M., Skärlén, Å., Cacciani, N., Braun,
821 T., Larsson, L., and Linke, W.A. (2020). Maintenance of sarcomeric integrity in adult muscle cells
822 crucially depends on Z-disc anchored titin. *Nature Communications* 11, 4479–18.
- 823 Syme, D.A., and JOSEPHSON, R.K. (2002). How to build fast muscles: synchronous and
824 asynchronous designs. *Integr Comp Biol* 42, 762–770.
- 825 Szikora, S., Gajdos, T., Novák, T., Farkas, D., Földi, I., Lenart, P., Erdélyi, M., and Mihály, J. (2020).
826 Nanoscopy reveals the layered organization of the sarcomeric H-zone and I-band complexes. *The*
827 *Journal of Cell Biology* 219.
- 828 Taylor, K.A., Rahmani, H., Edwards, R.J., and Reedy, M.K. (2019). Insights into Actin-Myosin
829 Interactions within Muscle from 3D Electron Microscopy. *Int J Mol Sci* 20.
- 830 Tonino, P., Kiss, B., Strom, J., Methawasin, M., Smith, J.E., Kolb, J., Labeit, S., and Granzier, H.
831 (2017). The giant protein titin regulates the length of the striated muscle thick filament. *Nature*
832 *Communications* 8, 1041.
- 833 Tskhovrebova, L., and Trinick, J. (2003). Titin: properties and family relationships. *Nature Reviews*
834 *Molecular Cell Biology* 4, 679–689.
- 835 Tskhovrebova, L., and Trinick, J. (2012). Molecular rulers? *Curr Biol* 22, R317–R318.
- 836 Tskhovrebova, L., and Trinick, J. (2017). Titin and Nebulin in Thick and Thin Filament Length
837 Regulation. In *Fibrous Proteins: Structures and Mechanisms*, (Cham: Springer International
838 Publishing), pp. 285–318.
- 839 Weitkunat, M., and Schnorrer, F. (2014). A guide to study *Drosophila* muscle biology. *Methods* 68, 2–
840 14.
- 841
- 842

843 **Figure legends**

844 **Figure 1 – *Drosophila* titin domain organisation and nanobodies**

845 (A, C) Sallimus (A) and Projectin (C) flight muscle protein isoforms with the domains
846 recognised by the used nanobodies highlighted in different colours. (B, D) Single confocal
847 sections of flight muscle sarcomeres from adult hemi-thoraces stained for actin with
848 phalloidin (magenta) and the indicated SIs or Proj nanobodies directly coupled to Alexa488 or
849 Atto488 (green). The Z-disc is revealed by the prominent actin signal. Scale bars 5 μm .

850

851 **Figure 2 – Nanobody penetration**

852 (A, B) Adult hemi-thorax expressing Obscurin-GFP (green) in flight muscles stained with
853 phalloidin to label actin (magenta) and either SIs-Nano2-Alexa488 (A) or anti-Kettin antibody
854 (binding SIs-Ig16) (red), followed by secondary antibody coupled with Alexa488 (B). Three
855 different z-planes and x-z slice are shown. Note that nanobody (red arrowheads in A) and
856 GFP signals (green arrowheads) are visible in the entire z-stack, whereas the antibody signal
857 decays quickly in z-direction (red arrowheads in B). Scale bars 5 μm . (C) Fluorescence
858 detection decay length versus imaging depth for GFP, anti-Kettin and SIs-Nano2 (anti-Kettin
859 vs SIs-Nano2 comparison: p-value = 0.0001748, Mann-Whitney test).

860

861 **Figure 3 – *Drosophila* flight muscle DNA-PAINT imaging and automated extraction of**
862 **sarcomeric protein domain positions.**

863 (A) Concept of DNA-PAINT imaging of sarcomeres labelled with an oligo-conjugated
864 nanobody. Binding of the imager oligo to one nanobody results in a strong, detectable
865 intensity burst (t_2 , blink). (B) Schematic of a mounted intact *Drosophila* hemi-thorax in a
866 DNA-PAINT imaging chamber enabling TIRF illumination. Comparison of the diffraction-
867 limited and the super-resolved result illustrated in one hemi-thorax labelled with Proj-Nano29.
868 Note that the super-resolved image can readily resolve the two-bands flanking each Z-disc.

869 Scale bar 2 μm . (C) Automated image analysis for individual Z-discs detection (see Figure 3
870 Supplement 3 and Methods for details). Individual bands are detected automatically and their
871 center position is obtained using a Gaussian fit (bottom center). The distance between the
872 center of bands for tens of sarcomeres from a single hemi-thorax is then reported in a
873 histogram (bottom right). Scale bar 2 μm (top) and 0.5 μm (bottom).

874

875 **Figure 4 – Single-colour DNA-PAINT imaging of Sls and Proj domains**

876 (A) Left: representative DNA-PAINT images of myofibrils stained with two different Sls or
877 Proj nanobodies labelling two epitopes and imaged with the same fluorescent imager oligo.
878 The different Sls or Proj nanobody combinations are indicated above each image. Middle:
879 pseudo-coloured sum image centered around Z-discs resulting from one hemi-thorax. Right:
880 histogram of distances between bands centered around Z-discs with the respective nanobody
881 combinations indicated in green or magenta. Note that four bands can be readily distinguished
882 for all shown nanobody combinations. (B) Similar representations as in (A). However, the
883 positions of neighbouring Sls or Pro epitopes cannot be resolved in a single colour. Scale bar
884 1 μm .

885

886 **Figure 5 – Dual-colour DNA-PAINT imaging reveals staggered order of Sls and Proj**

887 (A) Left: representative DNA-PAINT image of a myofibril stained with two nanobodies
888 labelling Sls-Ig13/14 (Sls-Nano2) and Sls-Ig51/Fn2 epitopes (Sls-Nano42). Middle: sum
889 image centered around Z-discs resulting from one hemi-thorax. Right: histogram of distances
890 between bands centered around Z-discs (Sls-Ig13/14 in green, Sls-Ig51/Fn2 in magenta). (B).
891 Top: representative DNA-PAINT image of a myofibril stained with two nanobodies labelling
892 Proj-Ig5-8 (Proj-Nano30) and Proj-Fn1/2 (Proj-Nano29) epitopes, sum image and histograms
893 of distances between bands (Proj-Ig5-8 in green, Proj-Fn1-2 in magenta). Bottom:
894 representative myofibril stained for Proj-Fn1/2 (Proj-Nano29) and Proj-Ig27-Fn35 (Proj-

895 Nano33) epitopes, sum image and histogram of distances between bands centered around Z-
896 discs (Proj-Fn1/2 in magenta, Proj-Ig27-Fn35 in green) (C). Top: representative DNA-PAINT
897 image of a myofibril stained with two nanobodies labelling SlsIg49/50 (Sls-Nano39) and
898 Proj-Fn1/2 (Proj-Nano29) epitopes, sum image and histogram of distances between bands
899 centered around Z-discs (Sls-Ig49/50 in green, Proj-Fn1/2 in magenta). Bottom: same as top
900 for Sls-Ig51/Fn2 (Sls-Nano42) and Proj-Ig5-8 (Proj-Nano30) epitopes, sum image, histogram
901 of distances and plot showing the epitope positions from the Z-discs in the individual
902 sarcomeres analysed (bottom right, Sls-Ig51/Fn2 in magenta, Proj-Ig5-8 in green). Note that
903 in 42 of 45 cases the Proj-Ig5-8 (green) is closer to the Z-disc than Sls-Ig51/Fn2 (magenta).
904 Scale bar 250 nm.

905

906 **Figure 6 – Summary and model**

907 (A) A sarcomere displayed as a composite of two summed Sls nanobody bands (top) and four
908 summed Proj nanobody bands (bottom), each originating from one individual hemi-thorax
909 imaged. Note the overlay of the positions of both proteins. Scale bar is 200 nm. (B)
910 Distribution of the averaged distances from the Z-disc for all Sls and Proj epitopes measured
911 using bootstrapping (see Methods). (C) Cartoon model of the relative arrangement of Sls and
912 Proj within the flight muscle sarcomere. The positions of the measured Sls and Proj domains
913 are highlighted in colours. The zoomed regions illustrate the suggested staggered architecture
914 of the C-terminal Sls and the N-terminal Proj protein parts.

915

916

917

918 **Supplementary figure legends**

919 **Figure 1 – figure supplement 1**

920 **(A, B)** Genomic organisation of *sallimus* (A) and *projectin/bent* (B) genomic loci taken from
921 Flybase. Pink rectangles indicate exons, lines indicate introns. Above the genomic locus is the
922 rough position of respective protein domains indicated. The domains named in grey are
923 largely specific to leg or larval muscle and not expressed in flight muscles. This is also
924 indicated by the prominent flight muscle-specific splice junctions indicated in grey below the
925 genomic loci. Note that the spring-like PEVK domains in *sallimus* or *projectin* are spliced out
926 in flight muscles. This results in the respective Sallimus and Projection domain structure of
927 the flight muscle isoforms. **(C)** Single confocal sections of flight muscle sarcomeres stained
928 for actin with phalloidin (magenta) and the indicated Proj nanobodies directly coupled to
929 Atto488 (green). The Z-disc is revealed by the prominent actin signal. Scale bars 5 μm .

930

931

932 **Figure 2 – figure supplement 1**

933 Scatter plots of band mean intensity in a given flight muscle myofibril versus imaging depth.
934 Dashed lines are the exponential decay fits for each hemi-thorax (individual decay lengths
935 obtained from the fits are reported in Figure 2C). GFP in green, anti-Kettin in orange and Sls-
936 Nano2 in blue.

937

938 **Figure 2 – figure supplement 2**

939 **(A, B)** Flight muscles of adult hemi-thoraces stained with phalloidin (red) and either Sls-
940 Nano2-STAR RED 9 (magenta) together with anti-Kettin antibody and secondary antibody
941 with Alexa488 (green) (A) or Sls-Nano2-Alexa488 (green) and anti-Kettin antibody with
942 Alexa633 (magenta) (B). Three different z-planes and x-z slice are shown. Note that in both

943 examples the nanobody penetrated the entire z-stack, whereas the antibody signal decays
944 quickly in z-direction. Scale bars 5 μm .

945

946 **Figure 3 – figure supplement 1(A)** Schemes illustrating the different steps of sample
947 preparation. Thorax isolation, followed by PFA fixation and hemithorax preparation. Fixed
948 hemi-thoraces are stained with nanobodies and are mounted in a sample chamber in imager
949 solution positioning the flight muscles close to the coverslip to enable TIRF imaging. **(B)**
950 DNA-PAINT post-processing workflow. The single-molecule ‘blinking’ events are identified
951 using a threshold detection and the maximum is determined via a Gaussian fit. The
952 coordinates in time and space and other localisation properties are saved in a hdf5 file. The
953 hdf5 is then drift corrected and rendered using Picasso render.

954

955 **Figure 3 – figure supplement 2 – Data analysis workflow**

956 **(A)** Individual myofibrils are manually selected using the rectangular selection tool from
957 Picasso (Schnitzbauer et al., 2017). Scale bar 2 μm . **(B)** To limit localisation events arising
958 from multiple emitters that create artefacts (Lelek et al., 2021), localisations are filtered based
959 on the standard deviation of their Gaussian fits. Localisations kept are within a disc in the
960 standard deviation space (sx, sy), centered on the maximum of the distribution and of radius
961 0.2 pixel. Scale bars 0.5 μm . **(C)** Individual Z-discs are automatically detected (see Methods
962 for details). Scale bars 2 μm . **(D)** Individual bands generated by the accumulation of protein
963 epitopes are detected automatically and their center position is obtained using a Gaussian fit.
964 After a visual check of the automated detection result, the results are compiled for further
965 analysis.

966

967 **Figure 5 – figure supplement 1 – Dual-colour DNA-PAINT sarcomere quantifications**

968 Distance quantifications of the dual-colour DNA-PAINT data shown in Figure 5. Plots on the
969 left show the epitope distances from the Z-discs in each individual sarcomere analysed with
970 green and magenta colours indicating the respective nanobodies used. Plots on the right
971 display histograms plotting the distances in between the individual two nanobody epitopes in
972 each sarcomere. These are half the values from the plots on the left, as the organisations are
973 symmetric around the Z-discs.

974

975 **Figure 6 – figure supplement 1 – Distance between bands versus sarcomere length**

976 Scatter plot of distance between bands of nanobodies used in this study versus the individual
977 sarcomere length. The sarcomere length reported for nanobodies centered on a given Z-disc is
978 obtained by measuring half the distance between Z-discs located directly on the left and on
979 the right. Note that the distances between bands do not correlate with the slight variations in
980 sarcomere length.

981

982

A Sallimus domains and nanobody localisation in flight muscles

nanobodies

Sls-Nano2

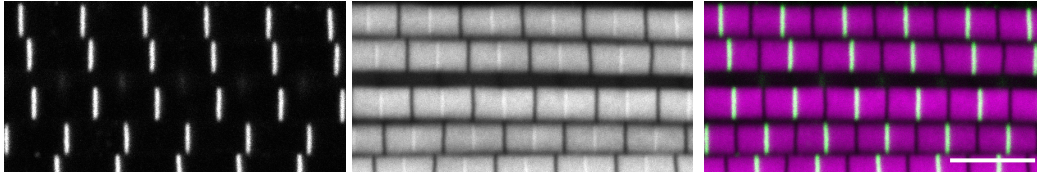
Sls-Nano39

Sls-Nano42, 48

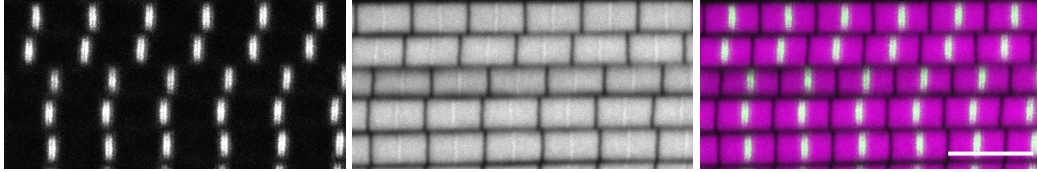
bioRxiv preprint doi: <https://doi.org/10.1101/2022.04.14.488306>; this version posted April 15, 2022. The copyright holder for this preprint (which was not certified by peer review) is the author/funder, who has granted bioRxiv a license to display the preprint in perpetuity. It is made available under aCC-BY 4.0 International license.

Sallimus flight muscle protein isoform

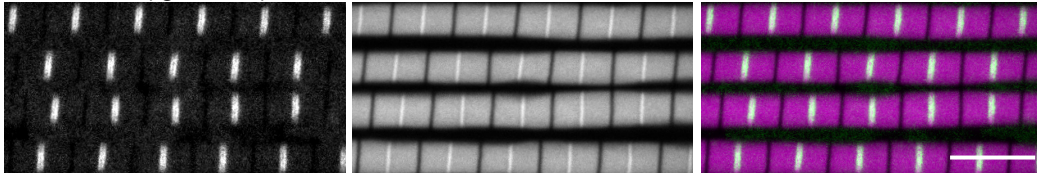
B Sls-Nano2(Ig13-14)-Alexa488 phalloidin-rhodamine



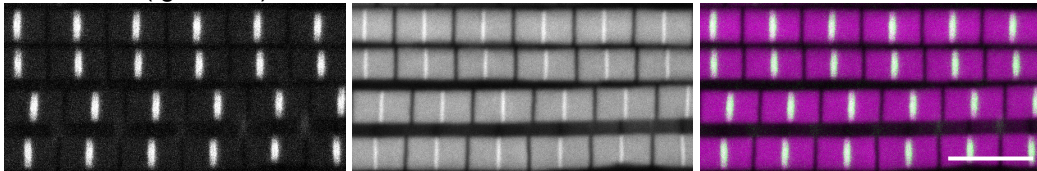
Sls-Nano39(Ig49-50)-Atto488



Sls-Nano42(Ig51-Fn2)-Alexa488



Sls-Nano48(Ig51-Fn2)-Atto488



C Projectin domains and nanobody localisation in flight muscles

nanobodies

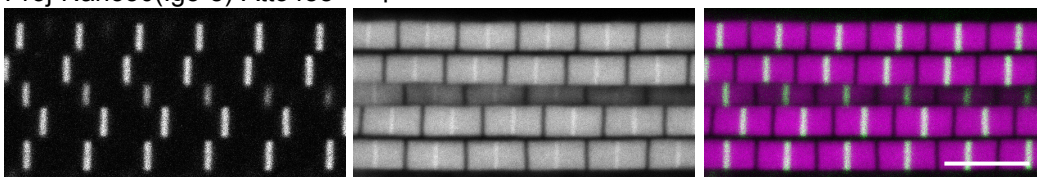
Proj-Nano30 Proj-Nano28, 29

Proj-Nano33 Proj-Nano34, 35, 37, 46

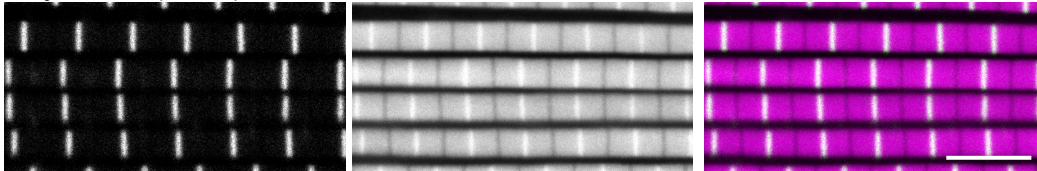


Projectin flight muscle protein isoform

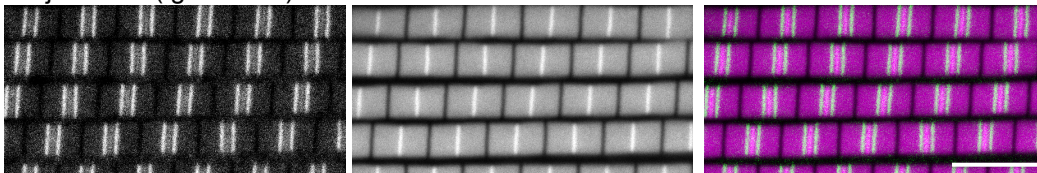
D Proj-Nano30(Ig5-8)-Atto488 phalloidin-rhodamine



Proj-Nano29(Fn1-2)-Alexa488



Proj-Nano33(Ig27-Fn35)-Atto488



Proj-Nano35(kinase)-Atto488

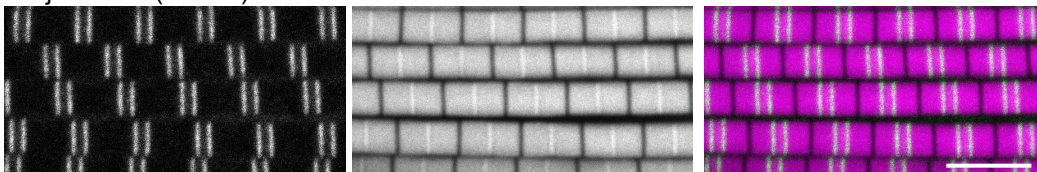
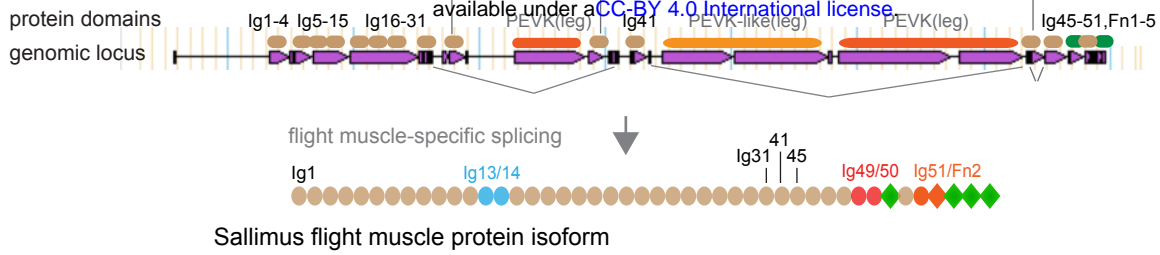


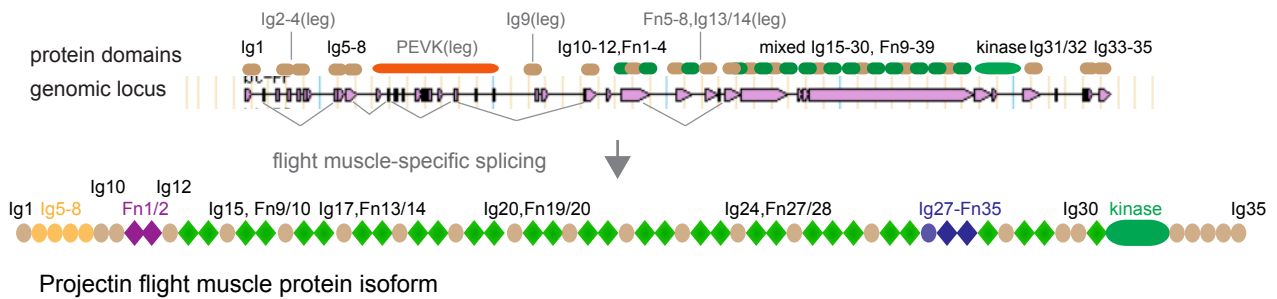
Figure 1

A Sallimus genome locus and flight muscle protein isoform

bioRxiv preprint doi: <https://doi.org/10.1101/2022.04.14.488306>; this version posted April 15, 2022. The copyright holder for this preprint (which was not certified by peer review) is the author/funder, who has granted bioRxiv a license to display the preprint in perpetuity. It is made available under a [CC-BY 4.0 International license](#).

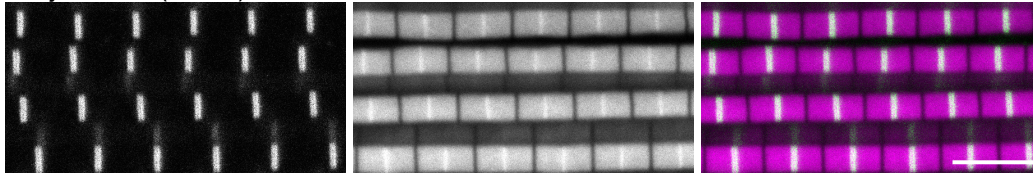


B Projectin genome locus and flight muscle protein isoform

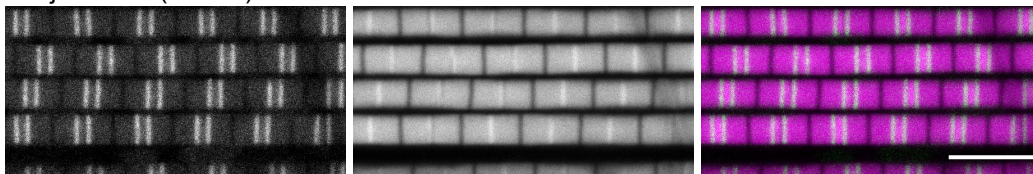


C Projectin nanobody localisation in flight muscles

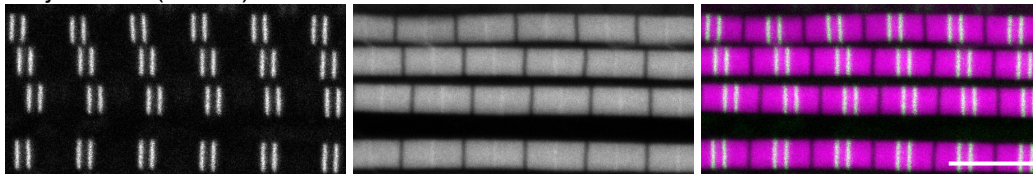
Proj-Nano28(Fn1-2)-Atto488



Proj-Nano34(kinase)-Atto488



Proj-Nano37(kinase)-Atto488



Proj-Nano46(kinase)-Atto488

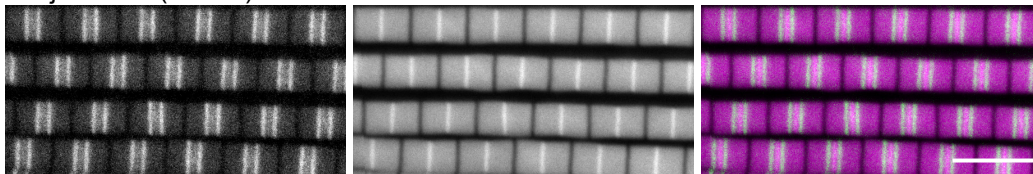
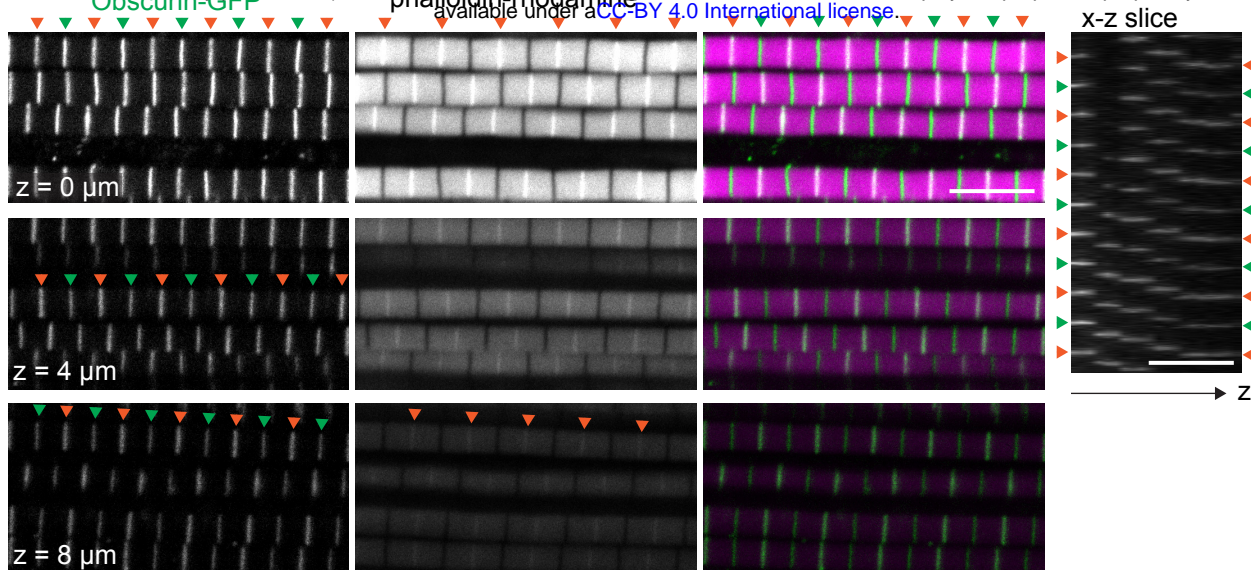


Figure 1 - figure supplement 1

A nanobody penetration in flight muscles - compared to endogenous GFP

bioRxiv preprint doi: <https://doi.org/10.1101/2022.04.14.488306>; this version posted April 15, 2022. The copyright holder for this preprint (which was not certified by peer review) is the author/funder, who has granted bioRxiv a license to display the preprint in perpetuity. It is made available under aCC-BY 4.0 International license.



B antibody penetration in flight muscles - compared to endogenous GFP

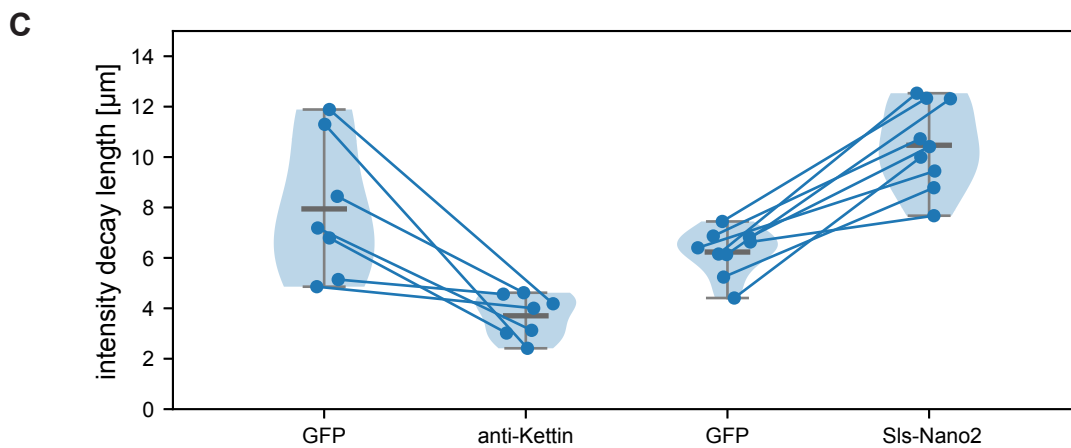
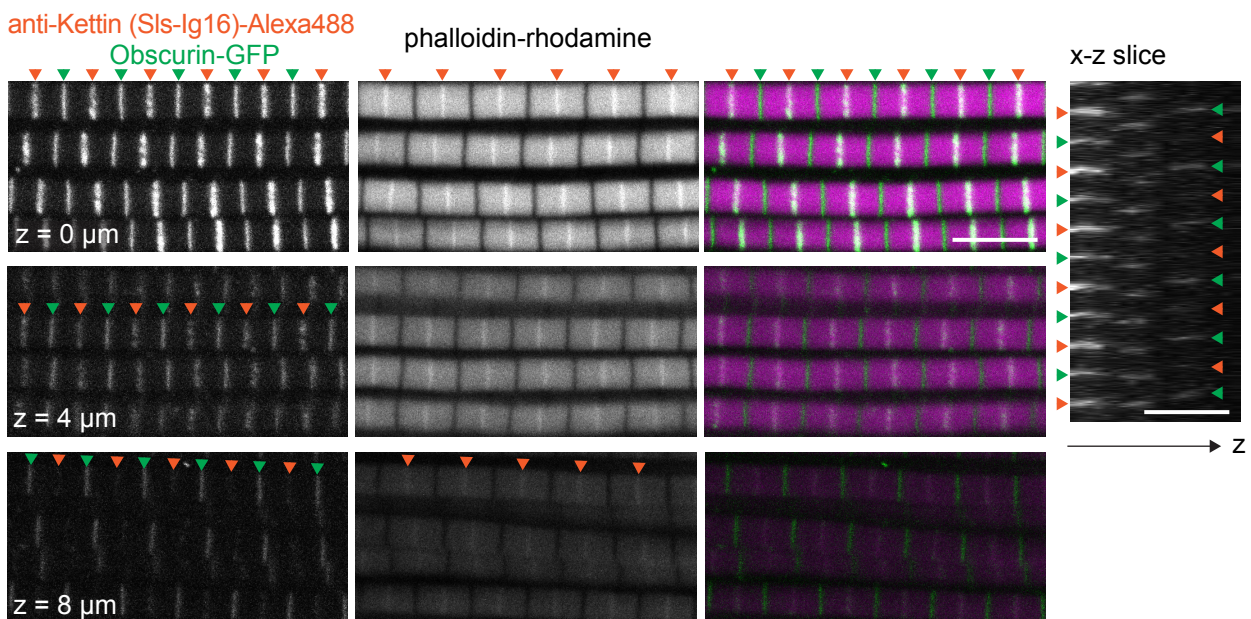


Figure 2

Extraction of fluorescence detection decay length

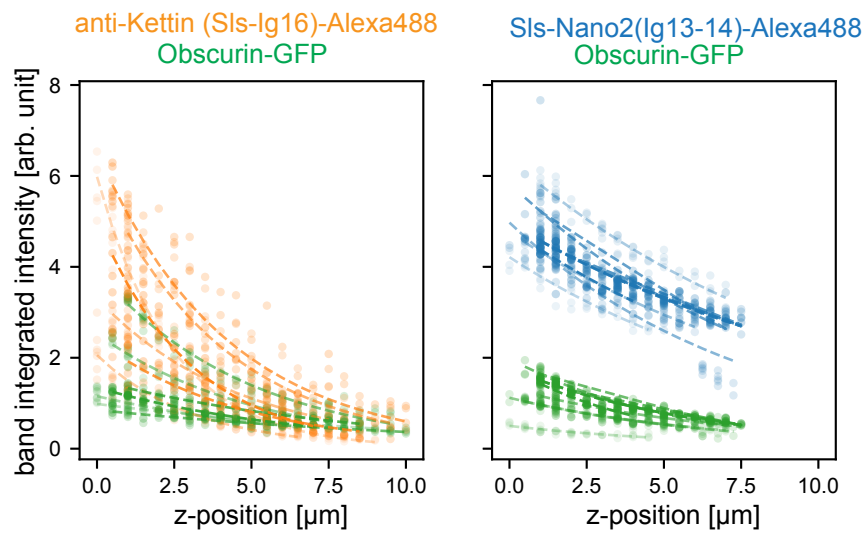


Figure 2 - figure supplement 1

A nanobody penetration in flight muscles - compared to antibody

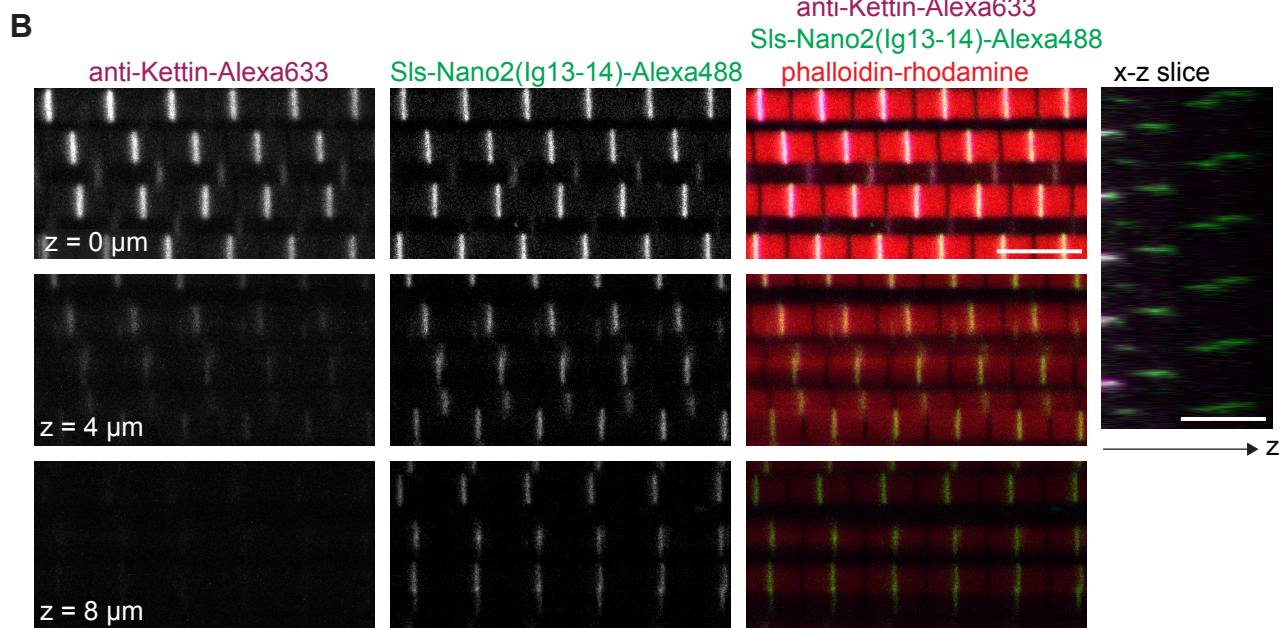
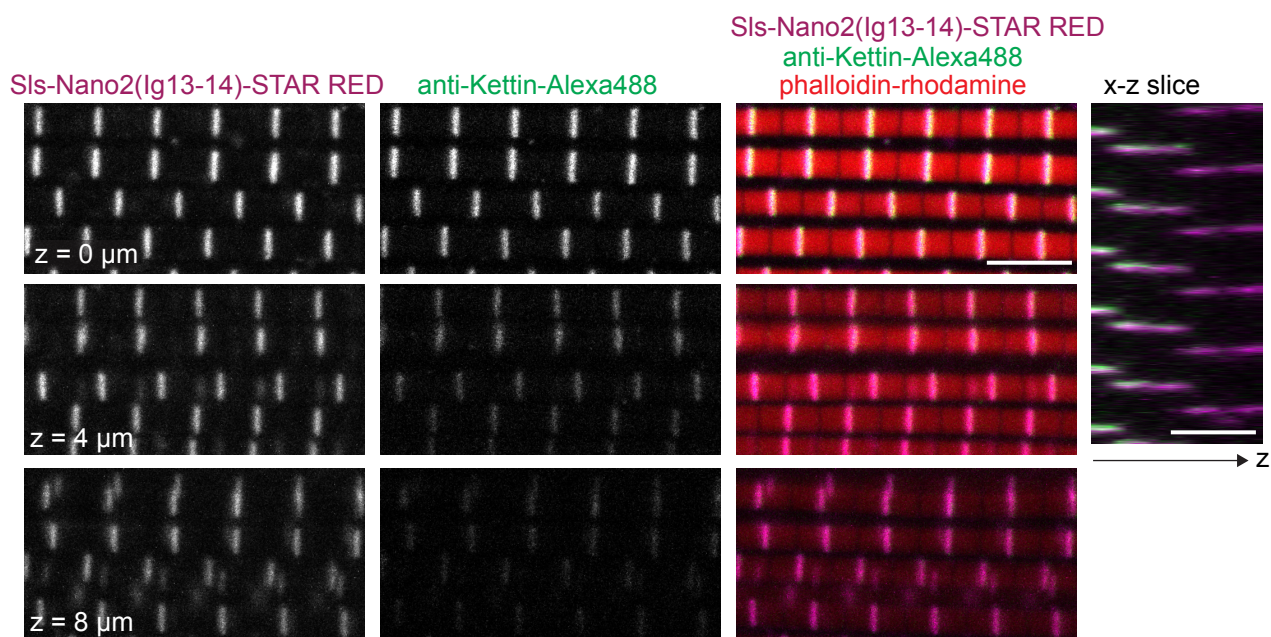
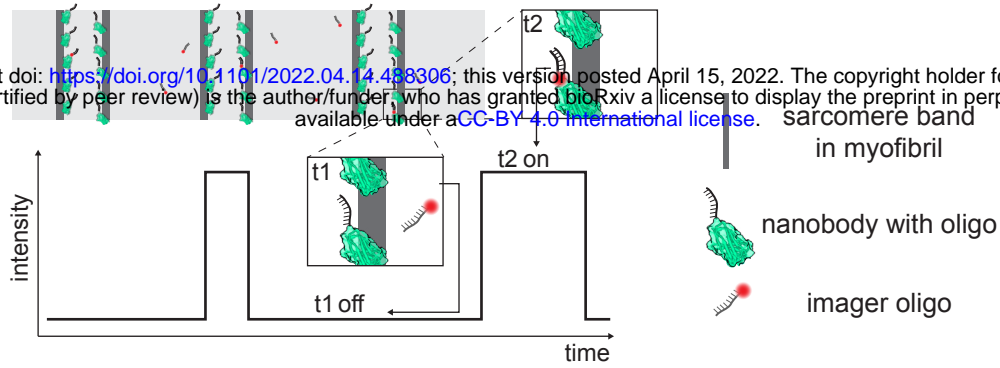


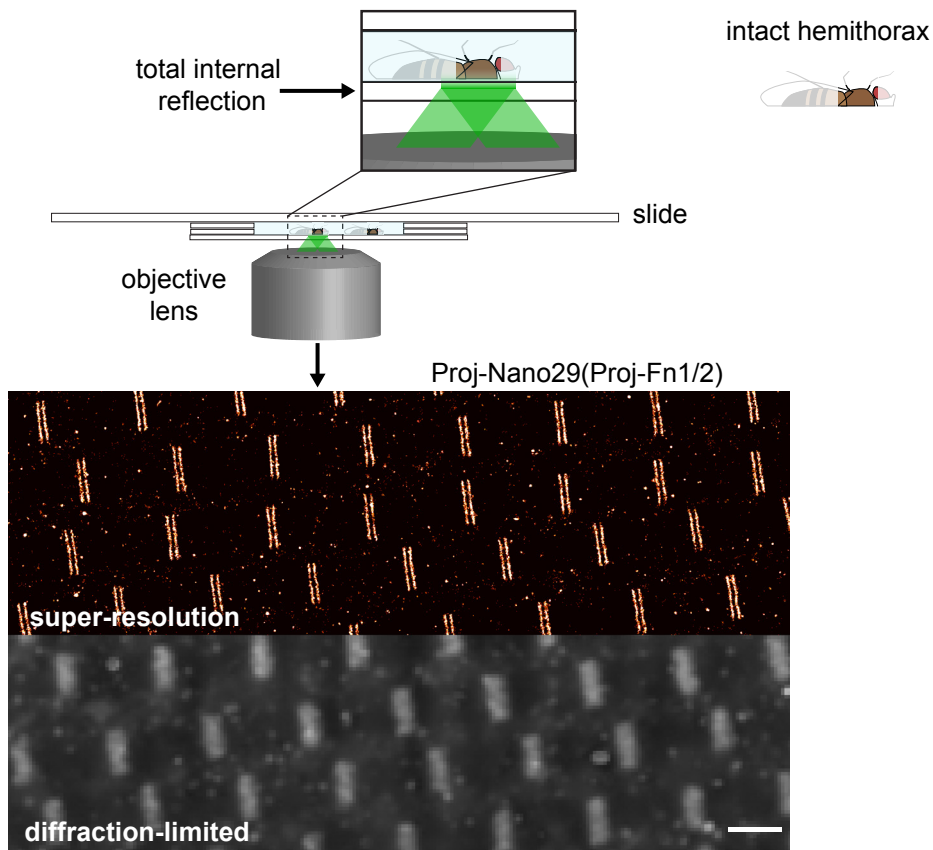
Figure 2 figure supplement 2

A Concept of DNA-PAINT

bioRxiv preprint doi: <https://doi.org/10.1101/2022.04.14.488306>; this version posted April 15, 2022. The copyright holder for this preprint (which was not certified by peer review) is the author/funder, who has granted bioRxiv a license to display the preprint in perpetuity. It is made available under a [CC-BY 4.0 International license](https://creativecommons.org/licenses/by/4.0/).



B In situ flight muscle imaging with TIRF



C Automated analysis

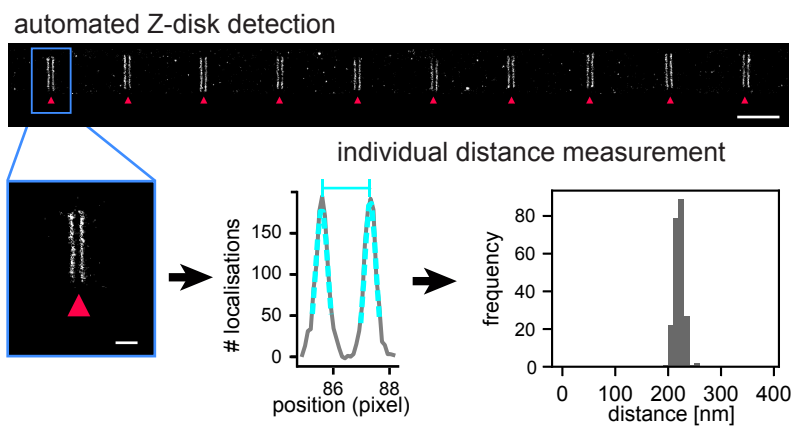
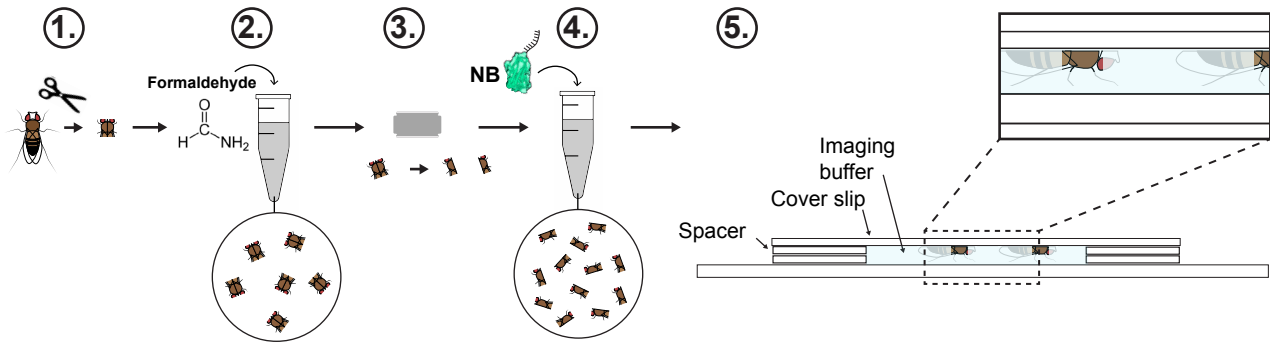


Figure 3

A Sample preparation

1. Thorax isolation by cutting head, wings and abdomen
2. Thorax fixation
3. Hemi-thorax isolation by cutting with a microtome knife
4. Staining with nanobodies
5. Mounting on sample chamber



B Super-resolution microscopy imaging & post processing

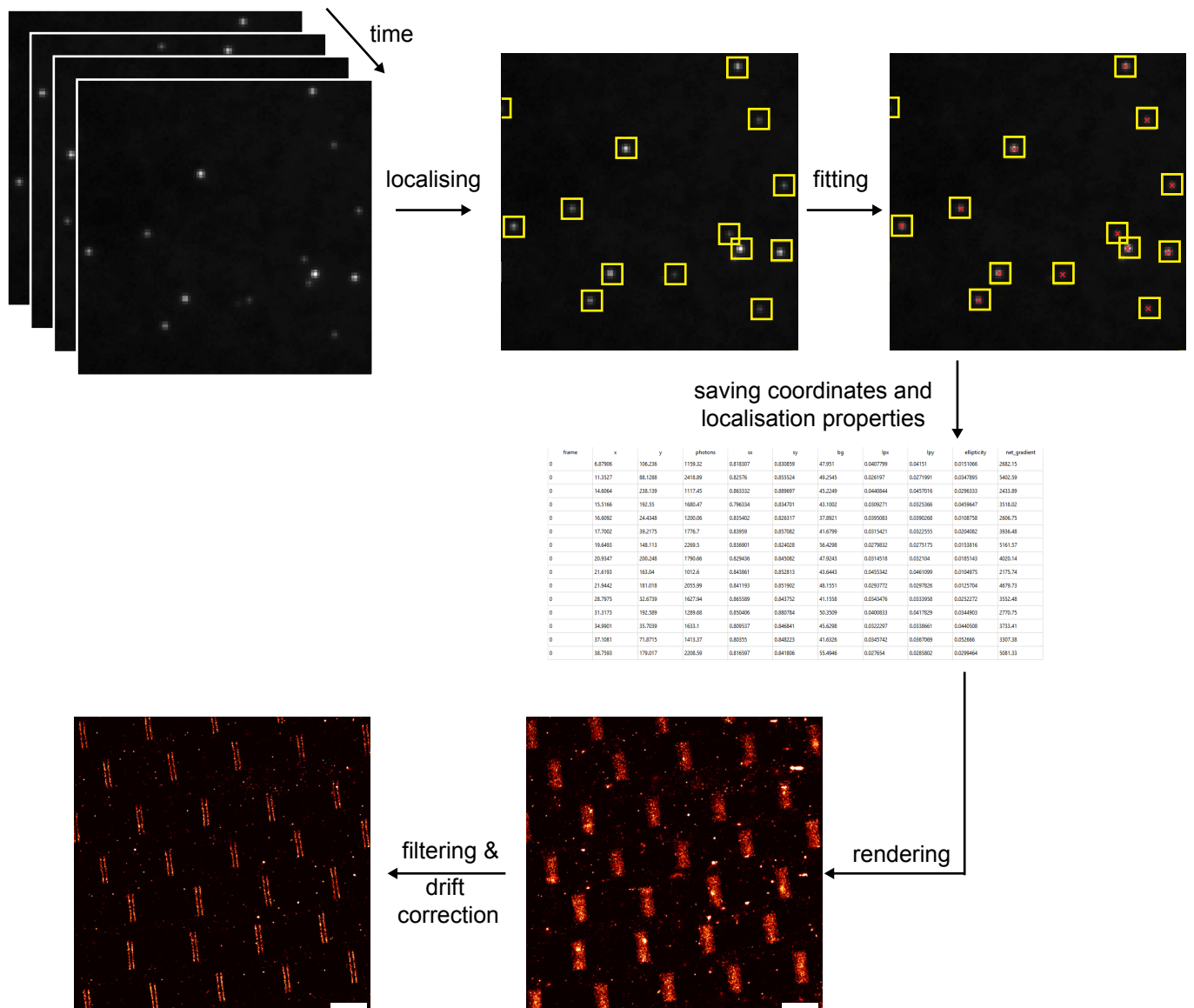


Figure 3 - figure supplement 1

Data analysis workflow

bioRxiv preprint doi: <https://doi.org/10.1101/2022.04.14.488306>; this version posted April 15, 2022. The copyright holder for this preprint (which was not certified by peer review) is the author/funder, who has granted bioRxiv a license to display the preprint in perpetuity. It is made available under aCC-BY 4.0 International license.

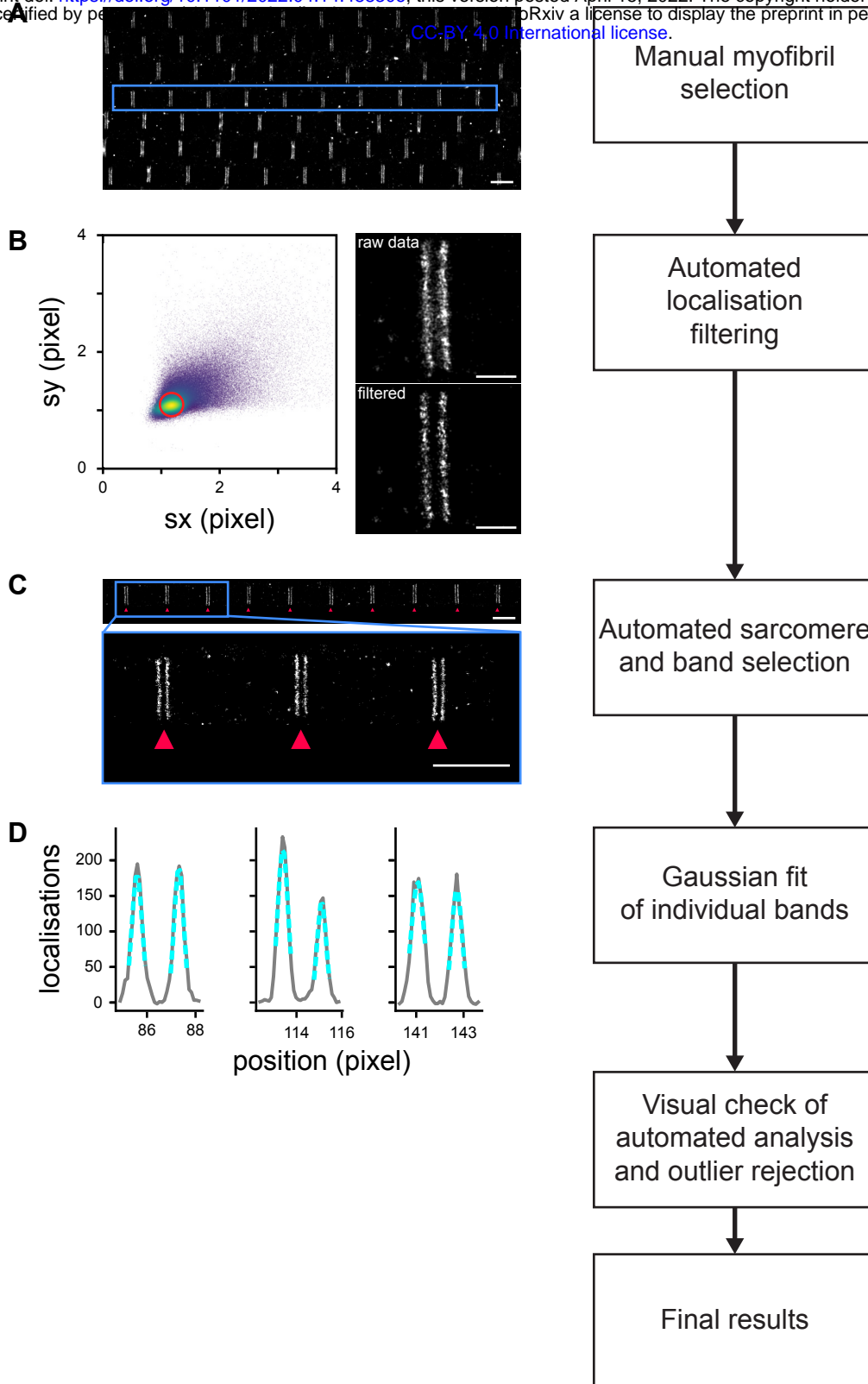
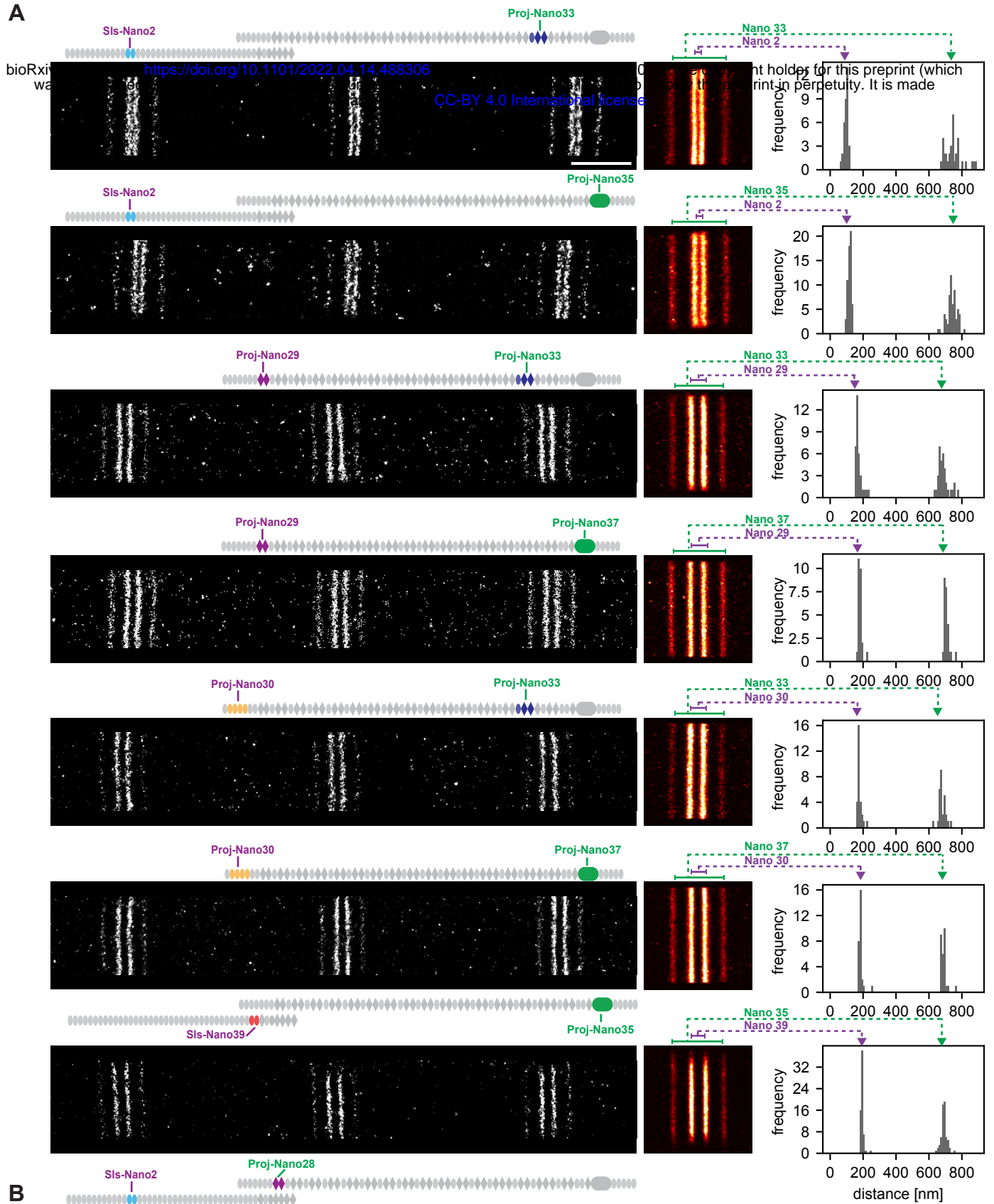
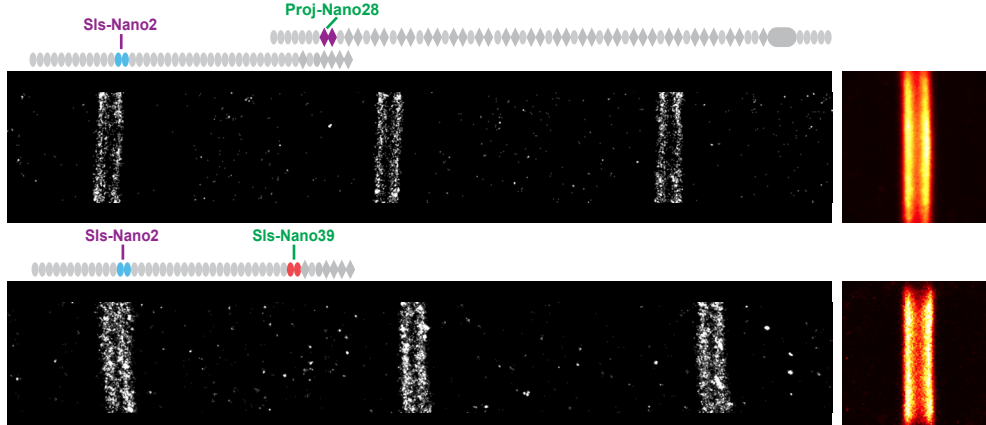
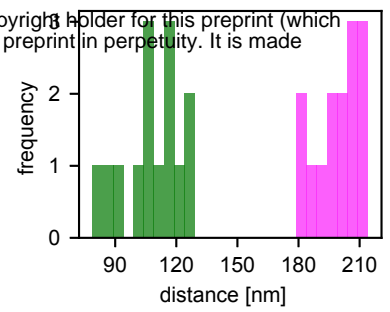
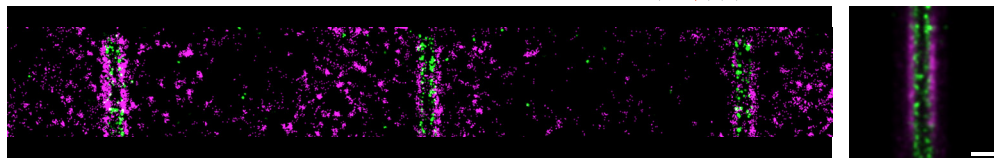


Figure 3 - figure supplement 2

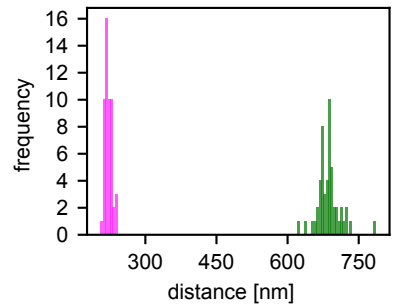
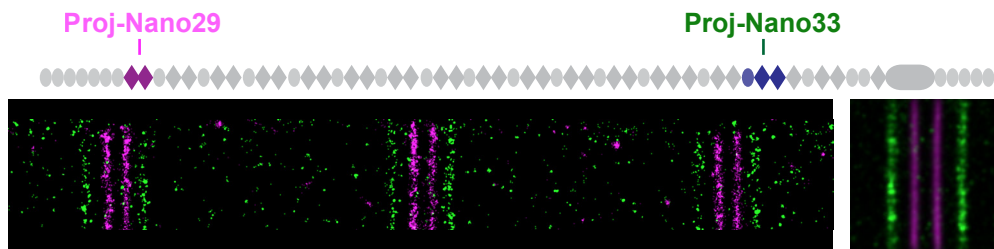
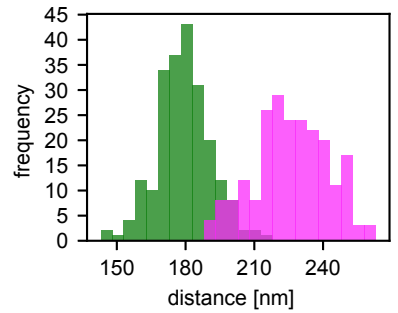
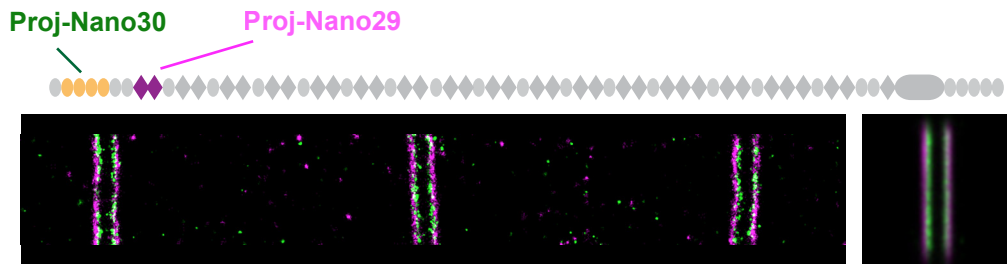
A**B****Figure 4**

A Length of Sallimus

bioRxiv preprint doi: <https://doi.org/10.1101/2022.04.14.488306>; this version posted April 15, 2022. The copyright holder for this preprint (which was not certified by peer review) is the author/funder, who has granted bioRxiv a license to display the preprint in perpetuity. It is made available under aCC-BY 4.0 International license.



B Elongated structure of Projectin



C Staggered order of Sallimus and Projectin

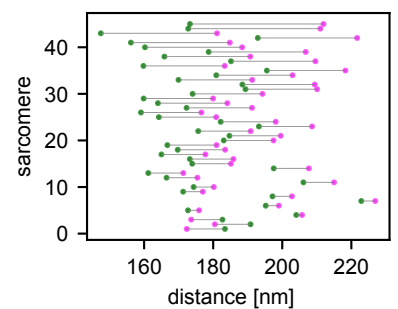
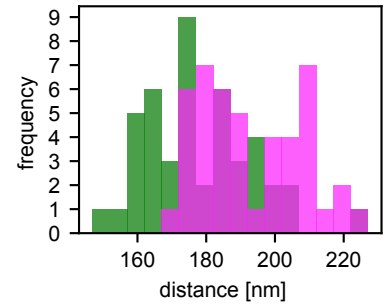
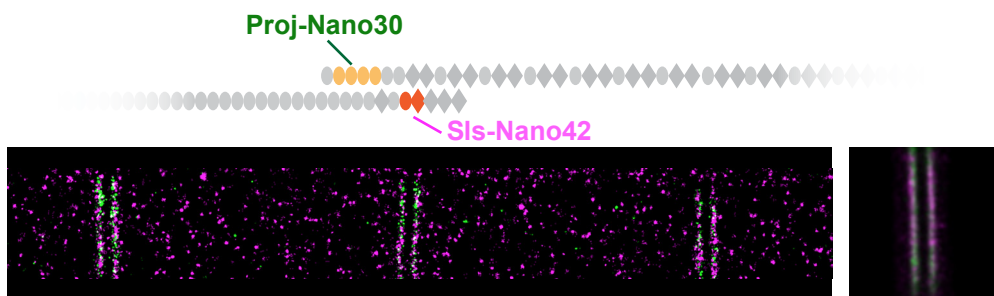
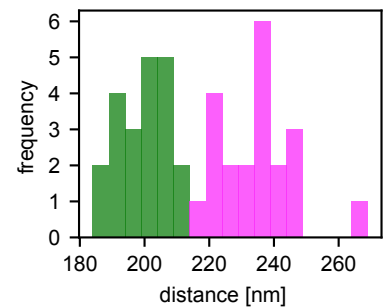
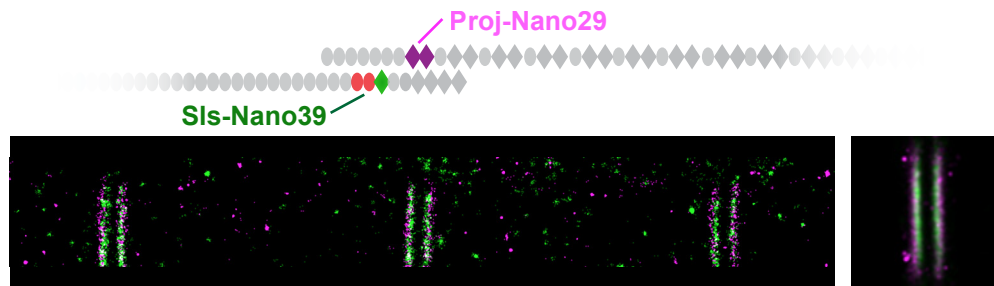


Figure 5

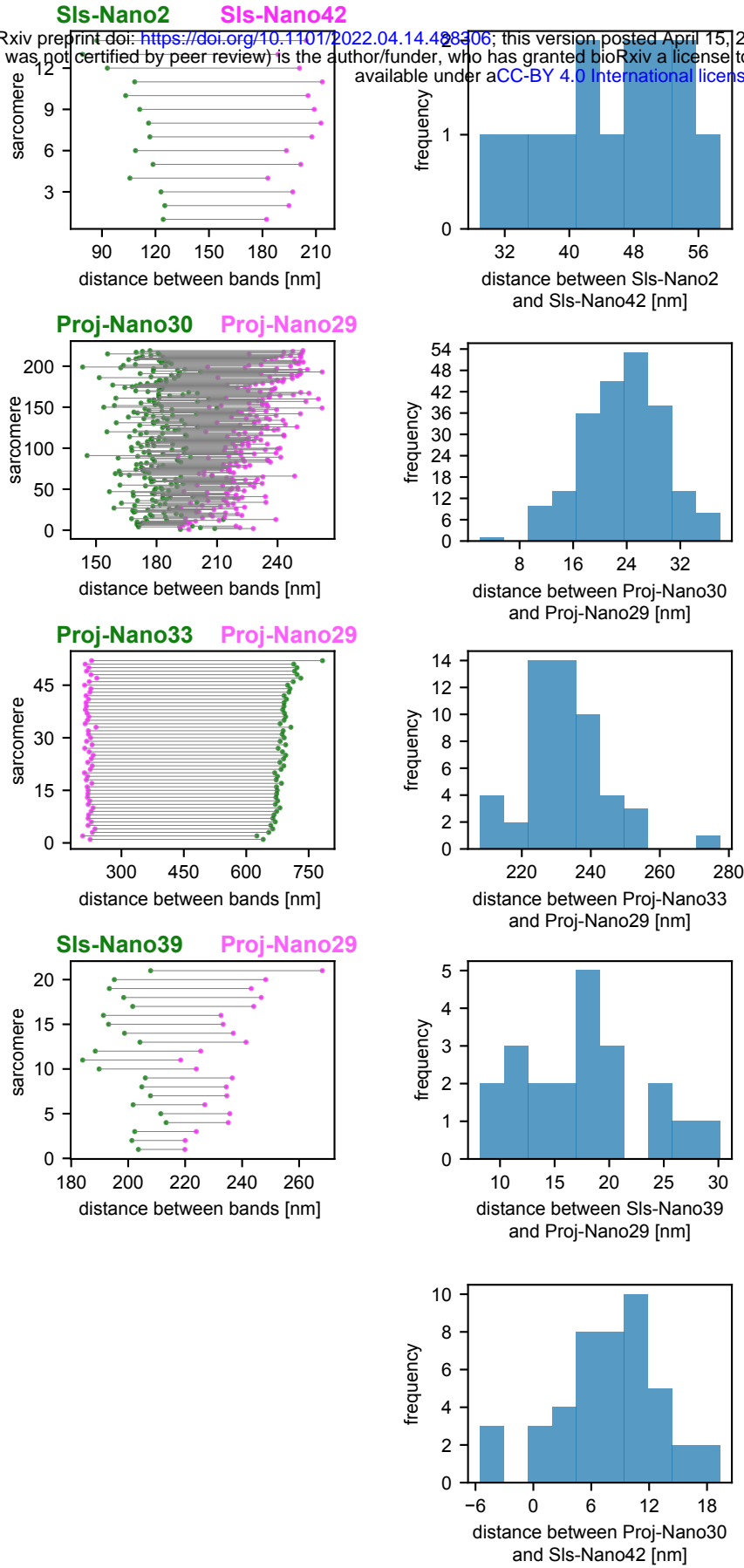


Figure 5 - figure supplement 1

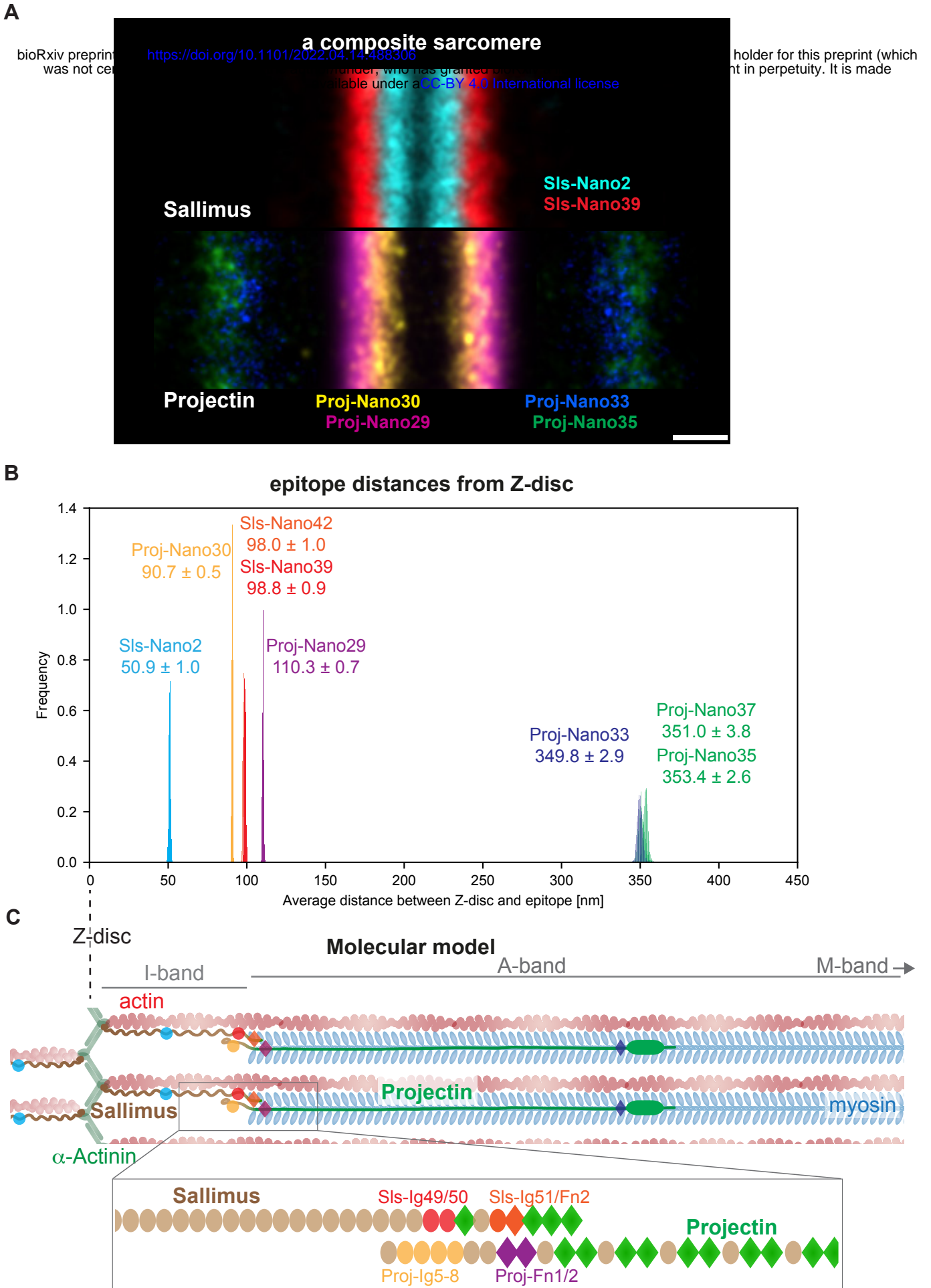


Figure 6

Distance between bands versus sarcomere length

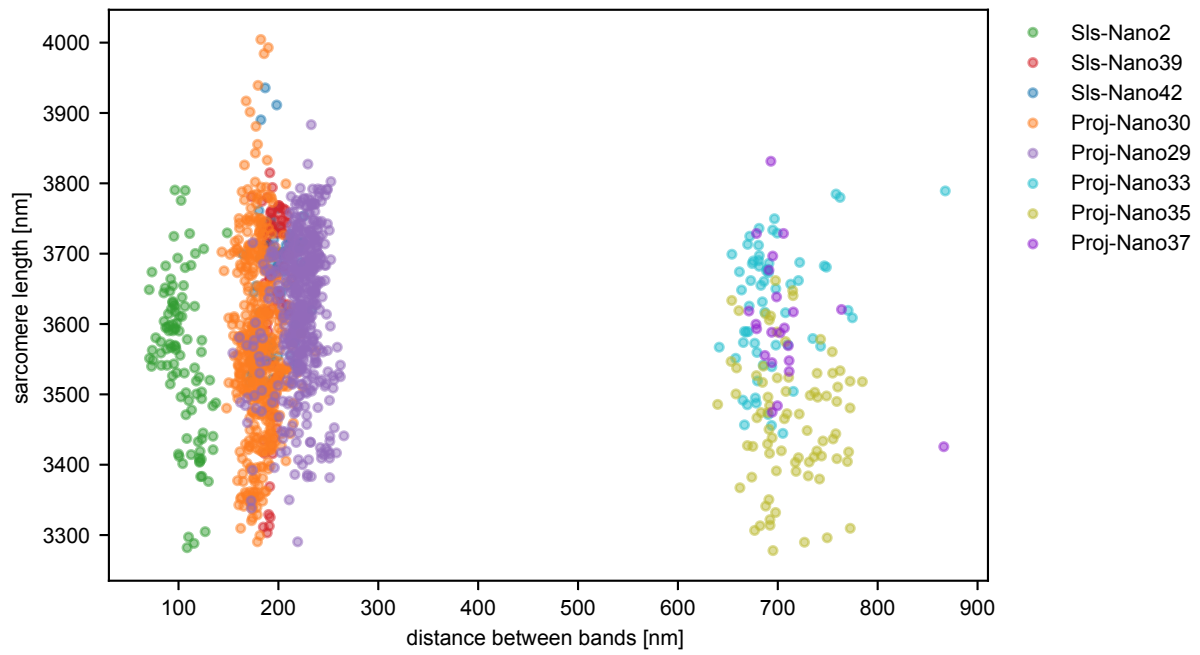


Figure 6 - figure supplement 1